TNF

Technisch-Naturwissenschaftliche
Fakultät

Beam Optics Simulations and Thermal Shielding for the AEGIS Antihydrogen Experiment

MASTERARBEIT

zur Erlangung des akademischen Grades

Diplom-Ingenieur

im Masterstudium

TECHNISCHE PHYSIK

Eingereicht von:
Sebastian Lehner, BSc.

Angefertigt am:
Institute of Experimental Physics (JKU)
Stefan-Meyer Intstitute for Subatomic Physics (ÖAW)

Beurteilung:
Prof. Dr. Eberhard Widmann

Mitwirkung:
Prof. Dr. Peter Bauer (Zweitgutachter)
Dr. Johann Zmeskal

Wien, Mai 2014

Eidesstattliche Erklärung

Ich erkläre an Eides statt, dass ich die vorliegende Masterarbeit selbstständig und ohne fremde Hilfe verfasst, andere als die angegebenen Quellen und Hilfsmittel nicht benutzt bzw. die wörtlich oder sinngemäß entnommenen Stellen als solche kenntlich gemacht habe.

Die vorliegende Masterarbeit ist mit dem elektronisch übermittelten Textdokument identisch.

Wien, 15.05.2014

Danksagung

ZUSAMMENFASSUNG

Das AEGIS (Antimatter Experiments: Gravity, Interferometry, Spectroscopy) Experiment an CERN's Antiproton Decelerator hat als Ziel die direkte Messung der gravitativen Wechselwirkung von Antiwasserstoff. Dies wäre ein neuer Test für die gegenwertige Theorie der Gravitation, die Allgemeine Relativitätstheorie. Möglicherweise würden solche Messungen auch aufschlussreich in kosmologischen Fragestellungen, wie Dunkle Materie, Dunkle Energie und Materie-Antimaterie Asymmetrie sein.

Der freie Fall eines Antiwasserstoffstrahls wird genutzt um die gravitative Beschleunigung mit einer Genauigkeit von 1 % zu bestimmen. Um das zu erreichen muss die Temperatur der für die Antiwasserstoffbildung verwendeten Antiprotonen bei etwa 0.1 K liegen. Dafür müssen die gefangenen Antiprotonen von gekühlten Wänden umgeben sein, da ansonsten Schwarzkörperstrahlung zu ihrer Erwärmung führen würde. Die gebildeten Atome werden von der Falle in ein deutlich wärmeres Strahlrohr geleitet. Thermische Strahlung aus diesem Bereich würde zu der Antiprotonenfalle gelangen. Eine gekühlte Verschlussklappe soll daher die Falle und das Strahlrohr trennen solange keine Atome aus der Falle extrahiert werden. In dieser Arbeit werden das Design und die Charakterisierung eines solchen Gerätes präsentiert.

Ein weiteres Thema dieser Arbeit hat mit der zweiten Zielsetzung von AEGIS zu tun. Neben den Gravitationsmessungen wird der Antiwasserstoffstrahl auch zur Untersuchung der Hyperfeinstruktur des Grundzustands genutzt werden. Damit soll die CPT Symmetrie mit bislang unerreichter Präzision getestet werden. Das Standardmodell ist invariant bezüglich der Vertauschung von Materie mit Antimaterie (C) und gleichzeitiger Inversion der Raum (P) und Zeit (T) Koordinaten. Diese CPT Symmetrie hielt bislang zahlreichen experimentellen Tests stand. Im Formalismus der Teilchenphysik lässt sie sich von fundamentalen Konzepten wie z.B. der Kausalität und Lorentz Invarianz ableiten. Die Entdeckung einer Verletzung der CPT Symmetrie würde daher ein erster Hinweis auf eine neue Physik (z.B.: String Theorie) sein, welche auf anderen Prinzipien basiert. Es wurde gezeigt, dass eine solche CPT-Verletzung zu einer Hyperfeinstruktur in Antiwasserstoff führen könnte, die von der bekannten in Wasserstoff abweicht.

Für diese Messungen wird der AEGIS Antiwasserstoffstrahl durch einen Sextupol Magneten geleitet, der die Atome entweder fokussiert oder defokussiert, je nachdem wie der Spin des Positrons ausgerichtet ist. Nur die Fokussierten werden einen Mikrowellenresonator erreichen, der den Spin umdrehen kann und dabei einen Übergang von einem Hyperfeinzustand zum anderen induziert. Zu diesem Übergang kommt es nur wenn die Mikrowellenfrequenz auf die Übergangsfrequenz eingestellt ist. Nach dem Resonator werden die Atome, die keinen Übergang gemacht haben durch einen weiteren Sextupol Magneten auf einen Detektor fokussiert. Indem man die Zählrate in Abhängigkeit von der Mikrowellenfrequenz misst, kann man die Übergangsfrequenz bestimmen.

Für diesen Teil der Arbeit wurden Strahloptik Simulationen des Antiwasserstoffstrahls in magnetischen Sextupol Feldern durchgeführt. Ziel war, die Position und Feldstärke der Sextupol Magneten zu optimieren. Zusätzlich wurde untersucht, ob Fokussierung mit Sextupol Magneten auch im Gravitationsexperiment nützlich sein könnte.

ABSTRACT

The AEGIS (Antimatter Experiments: Gravity, Interferometry, Spectroscopy) experiment at CERN's Antiproton Decelerator aims at a direct measurement of the gravitational interaction of antihydrogen. This would be a novel test of the current theory of gravity, General Relativity. It may also provide new insights in cosmological questions like Dark Matter, Dark Energy and the matter-antimatter asymmetry.

Via a free fall experiment on a beam of antihydrogen atoms the gravitational acceleration will be determined with a precision of 1 %. The temperature of the antiprotons used for antihydrogen formation must be about 0.1 K to allow this precision. A cryogenic environment is mandatory to avoid heating of the trapped antiprotons through black body radiation. Along the antihydrogen beam line the temperature of the apparatus will be significantly higher and black body radiation would reach the trap. To avoid this a cryogenic shutter is foreseen that separates the trap and the beam line as long as no antihydrogen atoms leave the trap. In this thesis the design and characterization of a prototype for such a device are presented.

Another topic of this thesis deals with the second goal of AEGIS. Aside from the gravity measurements the antihydrogen beam will be used for ground state hyperfine spectroscopy. This intends to probe CPT symmetry with unprecedented precision.

The Standard Model of particle physics is invariant with respect to replacing matter by antimatter (C) and simultaneous inversion of space (P) and time (T) coordinates. This CPT symmetry was tested in numerous precision experiments. In the present formalism of particle physics it was found to be a consequence of fundamental concepts like e.g. causality and Lorentz invariance. Hence a violation of CPT symmetry would be a first glimpse at new physics (e.g. string theory) that is based on radically different principles. It was pointed that the ground state hyperfine splitting in antihydrogen may deviate from the known splitting in hydrogen as a result of CPT violation.

For these measurements the AEGIS antihydrogen beam will pass through a first sextupole magnet that either focuses or defocuses the atoms according to the spin orientation of their positron. Only the ones that are focused reach a microwave cavity that can induce a spin flip and therein a transition from one hyperfine state to another. This transition is only induced if the microwave in the cavity is tuned to the transition frequency. After the cavity the beam passes through another magnetic sextupole field that focuses the atoms that have not undergone a transition towards a detector. By measuring the count rate in dependence of the microwave frequency the transition frequency can be determined.

The task for this part of the thesis was to perform beam optics simulations of the antihydrogen beam in magnetic sextupole fields to find the ideal arrangement for the spectroscopy beam line. In addition it was studied whether the focusing properties of a sextupole magnet could be used to enhance the count rate in the gravity experiment.

Contents

1. Introduction

1.1. Dirac's Postulation of Antimatter

In 1928 Dirac provided a relativistic version of the Schrödinger equation and therein brought the fundamental concepts of Special Relativity and Quantum Mechanics in accordance. Through analysis of this so called Dirac equation he was able to predict that for each species of particle there should be an antiparticle. Already in 1932 C. Anderson found particles in cosmic rays that had exactly the properties that were expected from the electron's antiparticle. These particles indeed turned out to be anti-electrons and were called positrons.

The following section briefly describes how the Dirac equation can be obtained by constructing a quantum mechanical wave equation that is relativistic. As a first step energy and momentum are substituted by operators that act on wave functions like in non-relativistic Quantum Mechanics:

$$p \rightarrow -\imath\hbar\nabla \tag{1.1}$$

$$E \rightarrow \imath\hbar\frac{\partial}{\partial t}. \tag{1.2}$$

Applying this to the relativistic energy momentum relation[1]

$$E^2 = p^2 + m^2 \tag{1.3}$$

results in the Klein Gordon equation

$$-\hbar^2\frac{\partial^2}{\partial^2 t}\psi = (-\hbar^2\Delta + m)\psi \tag{1.4}$$

which is relativistic and of second order. From the second order in time derivative a problem related to physical interpretation of ψ arose. Multiplying (1.4) from the left with ψ^* and calculating the difference of the resulting equation with its own complex conjugate gives the following continuity equation:

$$\frac{\partial}{\partial t}\rho + \nabla\mathbf{j} = 0, \text{with } \rho = \frac{i\hbar}{2m}\Big(\psi^*\frac{\partial\psi}{\partial t} - \psi\frac{\partial\psi^*}{\partial t}\Big). \tag{1.5}$$

Since (1.4) is of second order in the time derivative it requires knowledge of $\psi(t)$ and $\frac{\partial\psi}{\partial t}$ to be solvable. Hence these quantities are arbitrary and therefore ρ can take negative

---

[1] In this chapter units are chosen such that c = 1.

8

values which is not allowed for a probability density. [1]

This problem was circumvented by Dirac's first order equation:

$$i\hbar\frac{\partial}{\partial t}\psi = (-i\hbar\alpha_i\nabla_i + m\beta)\psi \text{ with i = 1,2,3.} \tag{1.6}$$

It allows only positive definite probability densities. In order to determine the coefficients α_i and β accordance of (1.6) with (1.3) is demanded. Thus the solutions of (1.6) also have to yield (1.4). Using (1.6) the left hand side of (1.4) can be calculated to be:

$$-\hbar^2\frac{\partial^2}{\partial^2 t}\psi = (-i\hbar\alpha_i\nabla_i + m\beta)(-i\hbar\alpha_j\nabla_j + m\beta)\psi = \tag{1.7}$$

$$\left(-\hbar^2\alpha_i\nabla_i\alpha_j\nabla_j - (\alpha_i m\beta + m\beta\alpha_i)i\hbar\nabla_i + \beta^2 m^2\right)\psi. \tag{1.8}$$

Since the right hand sides of (1.4) and (1.8) have to be equal the following unitarity and anticommutator relations for the coefficients are obtained:

$$\begin{aligned}
\alpha_i^2 = \beta^2 &= 1 \\
\alpha_i\alpha_j + \alpha_j\alpha_i &= 0 \\
\alpha_i\beta + \beta\alpha_i &= 0.
\end{aligned} \tag{1.9}$$

This requires that α_i and β are matrices at least of size 4×4. For instance the following matrices are a possible choice that satisfy (1.9):

$$\beta = \begin{pmatrix} I_2 & 0 \\ 0 & -I_2 \end{pmatrix}, \ \alpha_i = \begin{pmatrix} 0 & \sigma_i \\ \sigma_i & 0 \end{pmatrix}, \tag{1.10}$$

where σ_i are the Pauli Matrices. Since the coefficients α_i and β are 4×4 matrices the wave function ψ has to be at least a four component vector which is usually referred to as a spinor due to its transformation properties.[2] Analysis of solutions of (1.6) shows that the four components of ψ can be interpreted as the spin up and down wave functions of a particle and its antiparticle.

Using (1.6) it can be shown that antiparticles have the same mass and spin but opposite internal quantum numbers like e.g. electrical charge.

1.2. The Weak Equivalence Principle and its Tests

One peculiarity of the present theory of gravity is that a particle's trajectory in a given gravitational field only depends on the field and the particle's initial position and velocity (if no other forces are present). No further particle properties are relevant. In General Relativity the trajectories of a particle in a gravitational field are geodesics in space time and are therefore rather a property of space time than of the particle. This universality of free fall is also referred to as the Weak Equivalence Principle (WEP) [3]:

---

[2]From Lorentz invariance it can be deduced systematically that ψ has to be at least a 4 component spinor (see Chapter 3 in [2]).

The weak equivalence principle (WEP) states that in a uniform gravitational field all objects, regardless of their composition, fall with precisely the same acceleration.

The term "Weak" indicates that it only applies when gravitational binding energy is negligible. Therefore it is distinguished from the more general Strong Equivalence Principle which includes self gravitating objects [3].

A wide variety of experimental tests of the WEP were performed and support it. Their precision is often expressed in terms of the Eötvös parameter, which describes to which extend the free fall acceleration $g_{1,2}$ is equal for two test masses:

$$\eta = 2 \times \frac{g_1 - g_2}{g_1 + g_2}. \tag{1.11}$$

Rotating torsion balance experiments using Beryllium and Titanium test masses have achieved a precision of $\eta = (0.3 \pm 1.8) \times 10^{-13}$ [3]. This type of experiment is frequently regarded as an indirect test of the WEP in the antimatter sector. Antiparticle mass contributions to a normal matter atom arise through vacuum polarization effects like the Lamb shift and QED corrections to the electrostatic self energy of the nucleus. Additionally it is known from deep inelastic scattering that the antiquark content of the quark sea inside a proton is about 10 % [2, 4]. The relative size of these contributions depends on the atomic number since the lepton to nucleon ratio varies as well as the binding energy of nuclei. Therefore differences in the gravitational free fall of hydrogen (g_H) and antihydrogen (g_{Hbar}) can be constrained by torsion balance experiments to [5]

$$\frac{g_H - g_{Hbar}}{g_H} < 10^{-9}. \tag{1.12}$$

This reasoning is criticized as it implicitly assumes that gravitational coupling for virtual particles is the same as for normal particles. It is argued that in this case gravity would also couple to vacuum fluctuations which would result in a cosmological constant that is by 120 orders of magnitude different from the observed value [6].

A further argument against gravitational anomalies of antimatter is based on cyclotron frequency measurements in Penning traps. In these experiments the cyclotron frequencies of protons and antiprotons were determined to be equal with a relative precision better than 10^{-10} [7]. If the gravitational interactions of the proton and antiproton are not equal the gravitational red-shift would lead to different cyclotron frequencies for these particles in a given B field [8]. According to this reasoning the gravitational acceleration of the proton (g) and of the antiproton ($\bar{g}$) have to be equal within the estimated bounds of $|1 - g/\bar{g}| < 5 \times 10^{-4}$. This argument was challenged for assuming CPT symmetry (see Section 1.3) in the context of gravity and the existence of a meaningful absolute gravitational potential. [9]

Another indirect argument to rule out a WEP violation for antimatter was brought forward by Morrison [10]. It can be illustrated by the following gedankenexperiment: an electron - positron pair is dropped by some height and therein gains kinetic energy. Then the pair annihilates into two γ's that are guided upwards and red-shifted due to

the gravitational field. When the γ's reach the point where the electron - positron pair was dropped they turn again into an electron - positron pair. It is argued that in this cyclic process energy is only conserved if the electron and the positron have the same gravitational interaction.

The Standard Model Extension (SME) is an effective field theory of the Standard Model (SM) and General Relativity which includes Lorentz and CPT violation in a consistent way. While the SME does not make any assumption on the underlying physics for the violations it allows to study their possible effects in experiments. However, violation of Lorentz and CPT symmetry are often regarded as possible signs for physics at the Planck scale ($m_P \simeq 10^{19}$ GeV) where a presently unknown theory of Quantum Gravity is expected to show up. Violations at an observable extend could not be excluded from present experimental data which gave rise to numerous precision experiments. Probing antimatter systems is a possible way to find such violations. In the context of the SME a different gravitational interaction of antiparticles is allowed and in particular it was shown that energy would be conserved in the gedankenexperiment as described above. [11]

From a more general perspective it is evident that the present understanding of the universe on the largest scales faces severe problems. Currently it is not possibly to explain the asymmetry of matter and antimatter in the universe [12]. Already Dirac speculated that this asymmetry might be just a local phenomenon in a globally symmetric universe [13]. Searches for significant amounts of antimatter in the universe were not successful. For instance colliding galaxy clusters do not exhibit the x-ray signature, which would be expected if different sorts of matter were involved [14]. From analysis of the Cosmic Microwave Background and Cosmic Diffuse Gamma spectrum the absence of antimatter regions in the observable universe is concluded [15]. Other prominent open questions in modern physics and cosmology are those concerning Dark Matter and Dark Energy which are both inherently related to gravity.

Under the assumption of gravitational repulsion of matter and antimatter solutions to the afore mentioned problems (asymmetry, Dark Matter, Dark Energy) are frequently brought forward [16–18]. Gravity and antimatter could be essential in each of these questions. In conclusion there are numerous reasons to investigate antimatter gravity experimentally in the lab.

Direct gravity experiments with charged antimatter particles failed due to the influence of electromagnetic stray fields. As cold antihydrogen atoms became available several experiments aim at making a direct measurement of antimatter gravity. A first result was obtained by the ALPHA collaboration [19]. In their experiment trapped antihydrogen atoms were released and the time and location of annihilations on the surrounding detectors was recorded. As a result the ratio of gravitational mass m_g and the inertial mass m_i of antihydrogen was constrained to:

$$-65 < \frac{m_g}{m_i} < 110 \qquad (1.13)$$

at a statistical significance level of 5 %. As authors of [19] state their result is to be regarded as a proof of concept and more precise experiments are required.

Another attempt to determine the gravitational free fall of antihydrogen is made by the AEGIS (Antihydrogen Experiment: Gravity, Interferometry, Spectroscopy) collaboration which aims at a precision of g_{Hbar} at the 1 % level. [20]

A third experiment at CERN that will examine antihydrogen gravity is GBAR. It is scheduled to start data taking in 2017 and will try to reach a precision of 10^{-3} in g_{Hbar}. [21]

1.3. CPT Symmetry and Searches for its Violation

Symmetries play a central role in many fields of particle physics. Symmetry in this context essentially means that the laws of physics are invariant with respect to some symmetry transformation. Demanding continuous symmetries like gauge symmetries is the guiding principle to introduce fundamental interactions to theories of free particles. Another important class of symmetries are discrete symmetries. Among them are:

- time reversal T: $t \to -t$

- parity P: $x \to -x$

- charge conjugation C: particle $\to$ antiparticle.

For free particles which can for example be described by Eq. (1.4) or Eq. (1.6) these symmetries are all valid. It was found in experiments that processes of weak interaction can violate all of these discrete symmetries and combinations of them except for the combination of CPT. In contrast to all other discrete symmetries CPT symmetry can be rigorously derived from mathematical principles, which may however not be fundamental in nature. This theoretical reasoning for CPT symmetry is known as the CPT theorem and was first published in the fifties by Lüders and Pauli [22, 23]. A modern version of it can be found in [24].

The CPT theorem states that any local and Lorentz invariant quantum field theory of point particles must be CPT symmetric. This implies that inertial masses of particles and antiparticles and the energy levels in hydrogen and $\overline{H}$ are identical. Currently the most precise test of CPT symmetry results from the mass comparison of the K^0 and $\overline{K^0}$ mesons (see Fig. 1.1). As pointed out above scenarios for CPT violation are known in many candidates for Quantum Gravity as these theories do not necessarily meet the prerequisites of the CPT theorem. For instance QED can be extended to a more general theory that allows CPT and Lorentz violations. The resulting theory is used to study how effects of eventual violations could show up in $\overline{H}$ experiments. The nature of these violations is restricted by demanding features like a conserved energy-momentum tensor, microcausality, gauge invariance and renormalizability. The magnitude of symmetry violations and the required experimental precision to find them can not be predicted by such theories. But it is possible to study how sensitive experiments are with respect to such violations. As a result hyperfine splitting of the $\overline{H}$ ground state is claimed to be an exceptionally sensitive probe for CPT violations. [25, 26]

In searches for any deviation from CPT symmetry due to physics at higher energy scales (e.g. string theory) it is the absolute value of a measured quantity that is relevant. Hence in Fig. 1.1 it is the left edge of the red bars that indicates the sensitivity. Also from this point of view hyperfine splitting of $\overline{\text{H}}$ is of considerable interest. [25, 27]

Moreover CPT violation is proposed to play a central role in the question of the cosmological matter - antimatter asymmetry [28].
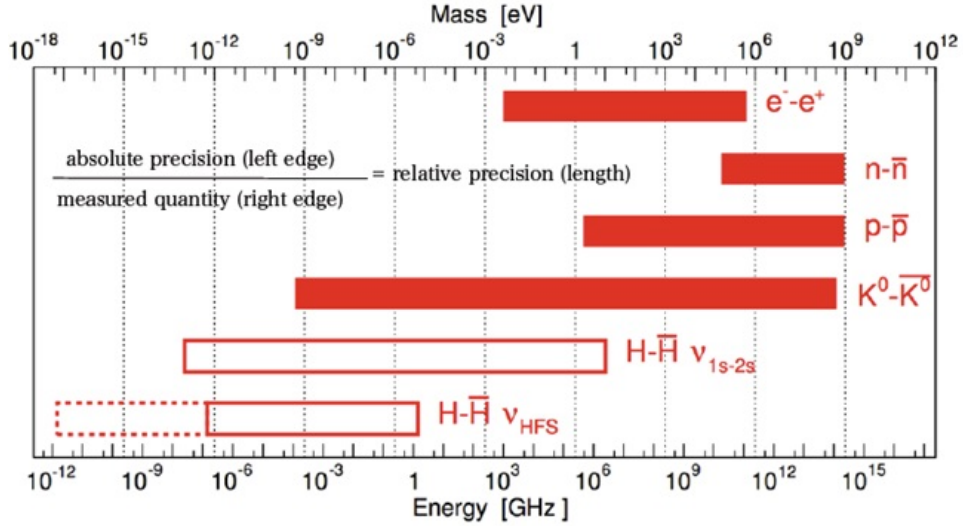
Figure 1.1.: Precision of some CPT tests compared with envisaged precision of $\overline{\text{H}}$ experiments. The right edge of the red bars indicates the measured quantity and the left edge the absolute precision of this measurement. The dashed line for H-$\overline{\text{H}}$ ν_{HFS} shows the theoretical potential of ground state hyperfine spectroscopy experiments. First generation experiments of this kind aim at the left edge of the solid bar which is slightly above 10^{-7} GHz. Taken from [29]

2. The AEGIS Experiment

The AEGIS collaboration has 70 members from 16 institutes. It aims at making a measurement of the gravitational free fall of antihydrogen ($\overline{H}$) at the 1 % level and therein providing a new test of the WEP in the antimatter sector. In addition Hyperfine Spectroscopy (HFS) of ground state $\overline{H}$ is foreseen which will put the CPT symmetry to the test. A third experiment will study laser excitation of Positronium (Ps) in electromagnetic fields which plays a crucial role in the $\overline{H}$ formation process (see 2.2).

2.1. The Antiproton Decelerator

The experiment will take place at CERN's Antiproton Decelerator (AD) which is currently the only facility that delivers cold antiprotons ($\overline{p}$'s). By guiding a 26 GeV proton beam from the Proton Synchrotron towards a static Iridium target $\overline{p}$'s are produced and separated from other collision products by magnetic fields. The resulting beam of 3.57 GeV $\overline{p}$'s is then injected into the AD ring (see Fig. 2.1). Here RF cavities decelerate the beam and form bunches of $\overline{p}$'s. As this reduces only longitudinal momentum the beam would become increasingly divergent during the deceleration process. Therefore the beam is cooled by means of Stochastic Cooling and Electron Cooling. At 5.3 MeV the $\overline{p}$'s are guided towards the central area of the ring where they pass through titanium degrader foils before reaching the AEGIS $\overline{p}$ traps.
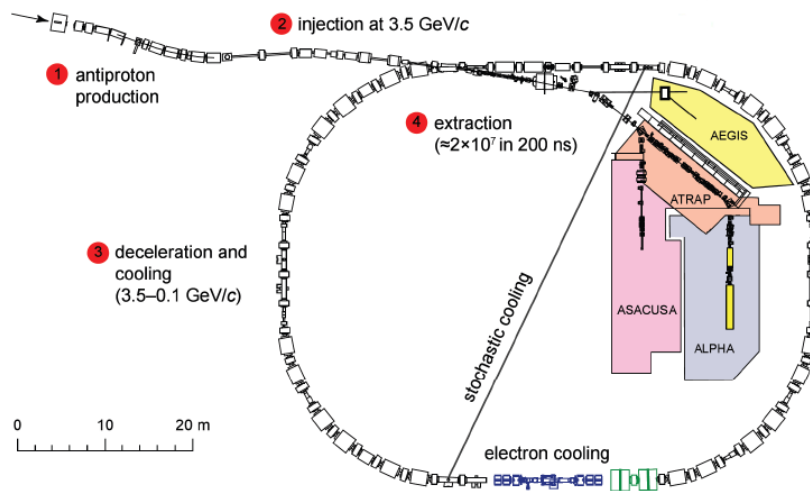

Figure 2.1.: Plan of the AD facility. Adapted from [30]

14

2.2. Antihydrogen Production and Beam Formation

A key challenge for the experiment is to form a slow $\overline{H}$ beam in order to have a sufficiently large free fall in the deflectometer. This requirement can not be met with $\overline{H}$ formation techniques that rely on mixing positrons (e$^+$'s) and $\overline{p}$'s in nested traps. In such experiments the $\overline{p}$ plasma bounces back and forth through a cold e$^+$ plasma. Therein the $\overline{p}$ plasma is cooled at first and should then form $\overline{H}$ in a three body reaction of two e$^+$'s and a $\overline{p}$. This technique was found to be inadequate for the production of $\overline{H}$ atoms at less than 1 K by the ATHENA collaboration. The problem was that $\overline{H}$ atoms were formed before the $\overline{p}$'s were sufficiently cooled. [31]

Therefore AEGIS will use a readily cooled $\overline{p}$ plasma and guide a beam of Rydberg Positronium (Ps*, $n_{Ps} \simeq 18 - 25$) towards it to produce Rydberg antihydrogen ($\overline{H}^*$):

$$\overline{p} + Ps^* \rightarrow \overline{H}^* + e^-. \tag{2.1}$$

This way of $\overline{H}$ production is called "Resonant Charge Exchange" and it was demonstrated by the ATRAP experiment [32]. The highly excited $\overline{H}$ atoms are then accelerated by electric field gradients to form a beam on which the experiments are performed.
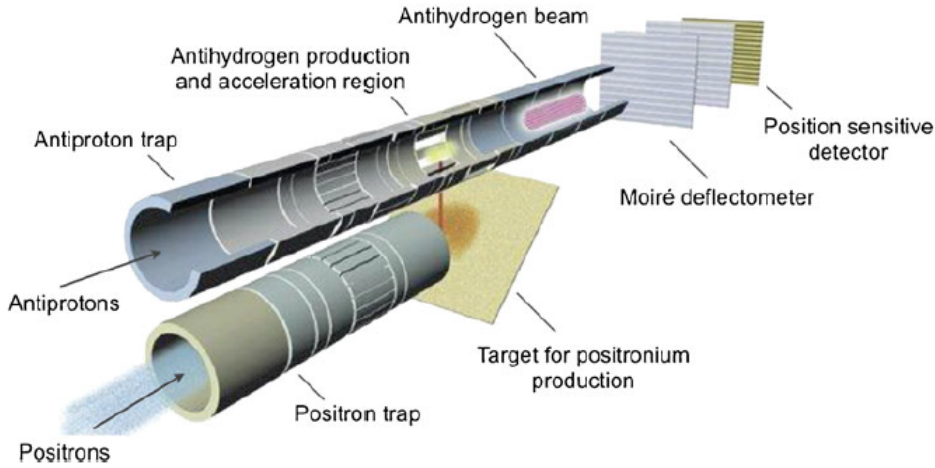
Figure 2.2.: Principle of the $\overline{H}$ beam production. Taken from [33]

In the following part the required steps from receiving $\overline{p}$'s from the AD to $\overline{H}$ beam formation are summarized. This section is widely based on [34].

2.2.1. Antiprotons

Per AD cycle 10^4 $\overline{p}$'s are captured from the degrader in a 5 T Malmberg-Penning trap (see Fig. 2.3). In such a trap a magnetic field along the direction of the incoming $\overline{p}$'s (axial) confines the plasma radially. The magnetic field is produced by a superconducting solenoid magnet at 4.3 K. Ring electrodes (visible as rings on the beam pipes in Fig. 2.2 and Fig. 2.4 right) at variable potentials are placed along the trap to confine

the plasma in the axial direction. For trapping the ring electrodes are operated at their maximum voltage of 20 kV which corresponds to the maximum energy of $\bar{p}$'s that can be caught.

e^-'s that are already trapped get heated by the arriving $\bar{p}$'s and efficiently cool themselves by emission of cyclotron radiation. $\bar{p}$'s are cooled through collisions with the e^-'s and reach an energy of some eV within tenths of a second. Cyclotron emission of $\bar{p}$'s is negligible due to their higher mass.

A residual gas pressure of 10^{-13} mbar will allow long enough storage times to stack several $\bar{p}$ bunches from consecutive AD cycles.

One ring electrode is radially divided into four independent parts that can exert a rotating electric field in order to radially compress the plasma. This method is known as the Rotating Wall [35]. Another technique to radially compress the plasma is known as Side Band cooling [34]. When cooling is finished the e^-'s are ejected from the trap by applying suitable voltage kicks with the electrodes that last for some 100 ns. This has no significant effect on the much heavier $\bar{p}$'s.

After the plasma of about 10^5 $\bar{p}$'s and 10^8 e^-'s reaches a sufficiently high density and is cold, it is guided towards a second Malmberg-Penning trap at 1 T (Fig. 2.3) where $\bar{H}$ atoms will be formed.
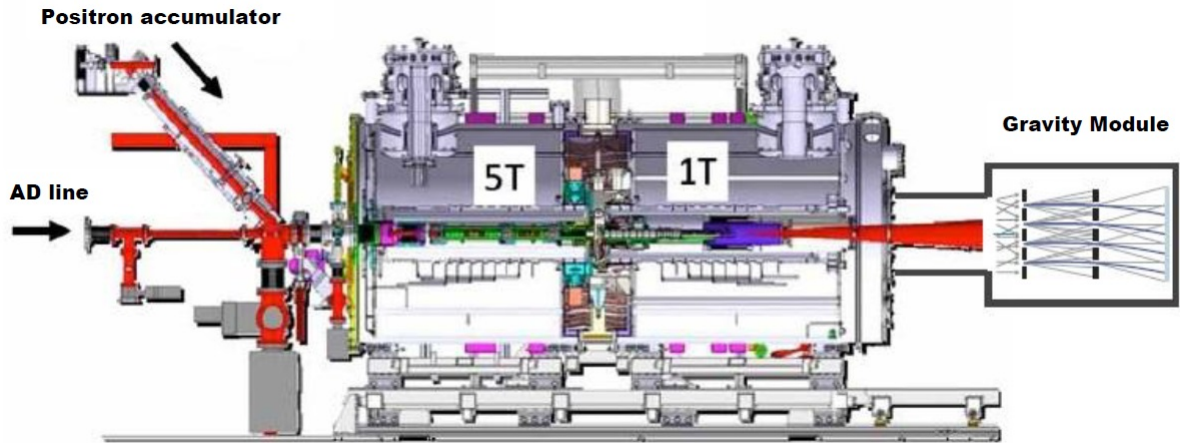
Figure 2.3.: Drawing of the AEGIS beam line and schematic depiction of the gravity module. Adapted from [36]

A second trap with lower magnetic field is used because cyclotron cooling of non-neutral plasmas (e.g. e^-'s) is known to be more efficient when the plasma is less magnetized. Additionally it is expected that high electromagnetic fields in the $\bar{H}$ formation zone would lead to unfavourable structure of $\bar{H}$ energy levels for the subsequent Stark acceleration. [37]

Figure 2.4.: Left: Beam line for incoming $\overline{p}$'s and e^+'s. On top of the rack the e^+'s source and accumulator are located. On the left hand side of the red ladder the transfer line to the 5 T magnet is visible. Beneath the e^+ source the beam line for the $\overline{p}$'s from the AD is shown. Middle: The 1 T (front) and 5 T magnets. The positron accumulator can be seen in the back (next to silver ladder). Right: The electrodes for the e^+'s (top) trap and $\overline{p}$ (bottom) trap in the 1 T region. Left & Middle: Photos taken by myself. Right: Taken from [38]
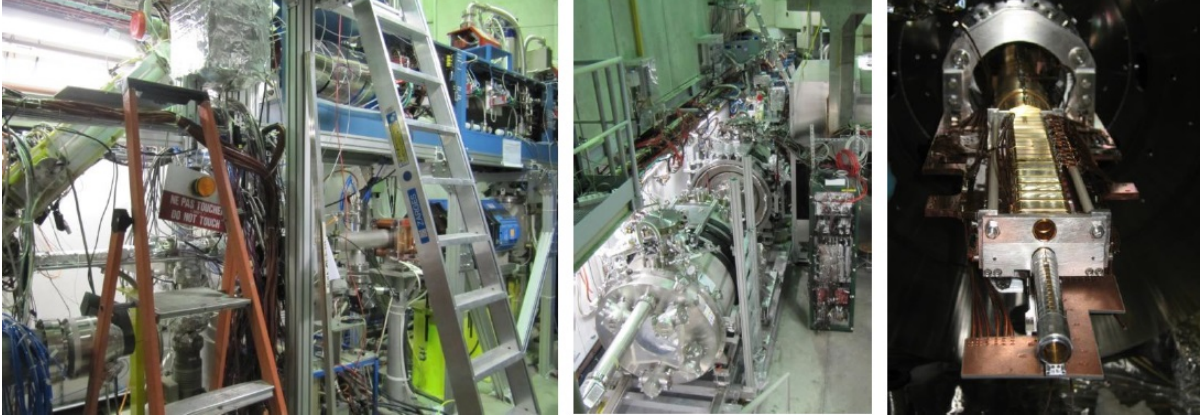
In the 1 T trap the plasma will be radially compressed again by Side Band Cooling and the Rotating Wall method.

The walls in the 1 T trap are cooled to 100 mK by a dilution refrigerator. After catching the ring electrodes in the 1 T trap (Fig. 2.4 right) form a harmonic axial potential (Penning trap) for the final cooling precess. In the 1 T field of the Penning trap the e^-'s modified cyclotron frequency (ω_+) is close to conventional (B field only) cyclotron frequency (ω_c):

$$\omega_+ \approx \omega_c \approx \frac{qB}{m}. \tag{2.2}$$

The lowest of the quantized energy levels

$$E_c = \hbar\omega_c(n + \frac{1}{2}) \tag{2.3}$$

is the one with $n = 0$. Its energy corresponds to a temperature of about 0.65 K. This sets the lower temperature limit for the radial cyclotron motion. The frequency corresponding to the axial modes is about 0.5 mK. Since these modes hardly radiate they require a further cooling mechanism. For this purpose Resistive Cooling will be applied. Here the axial motion of the e^-'s induces a current in an RLC circuit that is connected to two ring electrodes. This circuit is tuned to the axial frequency of the e^-'s. On resonance the resistance of the circuit turns the induced current into a voltage that counter acts the e^-'s axial oscillation. In this way the axial motion of e^-'s will reach 100 mK. As the e^-'s are in the lowest cyclotron mode they can not transfer energy of the cyclotron

motion to the p̄'s. Hence the p̄'s will be cooled to 100 mK which is the temperature associated to the axial oscillation of the e⁻'s.

During this process the number of e⁻'s is reduced again by applying voltage kicks. This will lead to a decrease in space charge. Therefore p̄'s that are displaced from the axial centre of the trap will experience a force towards the centre from the electrode's field that is no longer entirely compensated by the space charge. This results in heating and therefore the e⁻'s which are essential for cooling must be removed in a very controlled way.

2.2.2. Positrons

Independently of p̄ preparation a Surko-type accumulator (Fig. 2.4 left) will collect e⁺'s from a 50 mCi Na^{22} source. A small fraction of these isotropically emitted e⁺'s will be moderated by frozen Neon from 0.2 MeV to about 1 eV. A magnetic field guides these e⁺'s to the trap. Here again radial confinement is maintained via an axial magnetic field. Axial trapping is obtained with an electric potential that has a minimum on the opposite side of the trap entrance (see Fig. 2.5). In contrast to the traps discussed above this one contains Nitrogen. Like the electric potential also the pressure has its minimum at the back end of the trap. Arriving e⁺'s will pass through the trap and be reflected back and forth by the electric potential walls. During this process they lose energy in collisions with the N_2 molecules. Annihilation processes are much less likely than inelastic collisions. Finally the e⁺'s are stuck in the potential minimum where the N_2 pressure has a minimum in order to prevent reheating of readily trapped e⁺'s. Also in this trap segmented ring electrodes are used to apply the Rotating Wall method. More than 10^8 e⁺'s are expected to be delivered by the accumulator every 200-300 s.
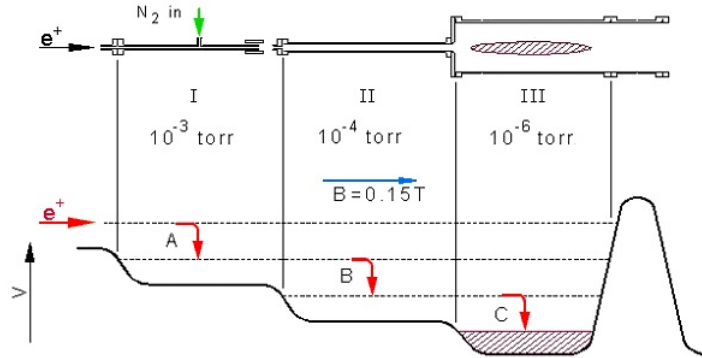

Figure 2.5.: Electric potential and pressure gradient in the e⁺ accumulator.
Taken from [39]

After cooling the e⁺'s are transferred to the 5 T trap. During accumulation and cooling a gate valve separates the e⁺ accumulator with the Nitrogen gas from the UHV region of the 5 T and 1 T traps. Before the gate valves are opened for the e⁺ transfer the

Nitrogen is pumped out. Suitable electric and magnetic fields guide the e^+ along the beam pipe to the 5 T magnet (Fig. 2.4 left).

The energy at arrival is in the order of several tens of eV. In the 5 T field the e^+'s cool themselves via cyclotron radiation until they reach thermal equilibrium with the inner surface of the trap at 4 K.

Next the e^+ plasma is transferred to the 1 T magnet where a so called "diocotron mode" is excited by ring electrodes to radially displace the plasma [37]. This way the e^+ can reach the off-axis e^+ trap in the 1 T field (Fig. 2.4 right). Here the e^+'s get accelerated by some kV towards a nano-porous silica material in which they will form Ps.

2.2.3. Positronium and Antihydrogen Production

Inside this material the e^+ is likely to thermalize and to capture an e^- to form Ps which can be re-emitted into the vacuum towards the $\bar{p}$ cloud (Fig. 2.2). The kinetic energy of Ps can be influenced via the size of the pores in which Ps behaves like a quantum mechanical particle in a box. The ideal velocity for $\overline{H}$ production is reached when the centre of mass velocity of the $\bar{p}$ - e^+ system is close to the orbital velocity of e^+ in Ps. This is the case for about 100-150 K which corresponds to a pore size of about 12 nm [40]. A cross section of up to $10^7 Å^2$ can be reached in the charge-exchange process [41].

Ps is produced either in the Para-Ps singlet state which has a life time of 125 ps or in one of the three Ortho-Ps triplet states which decay typically after 142 ns. The probability for each of these four states is equal. The life times given above are only valid for zero B fields. In the 1 T field the life time of Ortho-Ps is reduced to 15 ns. Due to the B field the $s_z = 0$ Ortho-Ps triplet state mixes with the short lived Para-Ps singlet state[1]. The reduced life time is still sufficient to laser excite the emerging Ps before annihilation. Para-Ps annihilates before laser excitation and can be detected in order to estimate the number of produced Ortho-Ps. [34]

Laser excitation is performed because it increases the cross section (σ) of the $\overline{H}$ formation process: $\sigma \propto n^4$. A Nd:YAG pump laser and a system of optical parametric generators and amplifiers delivers laser pulses of about 10 ns. For the two step transition the following pulses are used:

- $n_{Ps} = 1 \rightarrow n_{Ps} = 3$: $\lambda = 270$ nm, saturation energy: 2 μJ

- $n_{Ps} = 3 \rightarrow n_{Ps} = 18 - 25$: $\lambda = 1650\text{-}1700$ nm, saturation energy: 0.2 mJ.

Monte Carlo simulations show that the principal quantum number of $\overline{H}$ atoms ($n_{\overline{H}}$), that are produced by the above mentioned charge-exchange process, will be roughly proportional to n_{Ps}: $n_{\overline{H}} \approx \sqrt{2} n_{Ps}$. [43]

Finally the Ps will reach the $\bar{p}$'s through openings in the electrodes of the $\bar{p}$ trap (see Fig. 2.4 right) and form $\overline{H}$. As $\overline{H}$ is neutral it leaves the $\bar{p}$ trap isotropically with a

---

[1]See 11.43 and 11.61 in [42] for more details. A similar mixing will be encountered in Section 3.1 Eq. (3.8) for hyperfine states of Hydrogen.

velocity of about 50 m/s, corresponding to a temperature of about 100 mK. To form a beam so called Stark acceleration is used. In an external electric field the $\overline{\text{H}}$ energy levels split due to the Stark effect. To treat this problem theoretically usually parabolic quantum numbers are introduced. The relevant quantum number for the Stark effect is k, which can be defined by: $k = n_1 - n_2$. Here n_1 and n_2 are again parabolic quantum numbers that can take non-negative integer values and which are related to the spherical ones by $n = n_1 + n_2 + |m| + 1$. From these definitions it follows that k can take any value in steps of two in $[-(n - 1 - |m|), n - 1 - |m|]$. Using quantum mechanical perturbation theory the following shifted energies levels in hydrogen due to the Stark effect are obtained (in atomic units)[2]:

$$E = -\frac{1}{2n^2} + \frac{3}{2}kn\varepsilon. \tag{2.4}$$

Here ε denotes the electric field. From (2.4) the following force F on a (anti-) hydrogen atom is obtained: $F = -\frac{3}{2}kn\nabla\varepsilon$. About 50 % of $\overline{\text{H}}$'s will have the right sign of k and will be accelerated by an axial electric field gradient towards the experimental section. The other 50 % will be accelerated in the opposite direction and are lost. A higher final velocity will make the beam less divergent but also reduces the free fall in the experiment. Regarding these factors a velocity of about 400 m/s is envisaged.

Decay of $\overline{\text{H}}$ with $n \simeq 30$ takes typically 300 μs which would correspond to a flight distance of 12 cm (under the assumption that the $\overline{\text{H}}$ are as cold and slow as planned). This is well before either the spectroscopy or gravity experiment is reached . The energy levels of $\overline{\text{H}}$'s will be investigated by field ionization. For this purpose electrodes produce an electric field in the $\overline{\text{H}}$ flight path that will ionize all $\overline{\text{H}}$'s with n higher than a certain value and therein reduce the number of $\overline{\text{H}}$'s that can leave the source. The critical n value can be controlled via the applied voltage.

For the gravity experiment a low state of $\overline{\text{H}}$ is necessary to ensure that the free fall is not flawed by electromagnetic stray fields or by the recoil of radiative decays.

In case of HFS it is essential to have $\overline{\text{H}}$ in ground state since the cavity will be tuned to a hyperfine transition of this particular state (see Section 2.4). The decay of Rydberg $\overline{\text{H}}$ could be artificially accelerated by black body radiation. This effect is negligible in the cryogenic environment of the experiment that is required for $\overline{\text{p}}$ cooling. A possibility to use black body radiation is to have the beam pipes of the experimental section at higher temperatures. In order to protect the $\overline{\text{p}}$ trap from the associated black body radiation a cryogenic shutter at the exit of the trap could block the radiation. This shutter would have to be opened right before $\overline{\text{H}}$ is produced and extracted. The design and construction of a prototype of such a shutter is described in Chapter 4.

$\overline{\text{H}}$ production in the AEGIS apparatus is the key goal for the second half of 2014 when the AD is going to be back in operation after the general shut down at CERN. The next major step will be to optimize the process and to produce cold $\overline{\text{H}}$ which would allow to perform the experiments.

---

[2]For details see Problem 2.3 in [44].

2.3. Gravitational Free Fall and Deflectometry

A Moiré deflectometer is used to make a precise measurement of the free fall of the uncollimated $\overline{\text{H}}$ beam. It consists of two identical gratings and a position sensitive emulsion detector. These elements are all displaced along the beam axis by a distance L (see Fig. 2.2). The grating periodicity will be 40 μm and the slit width 12 μm. $\overline{\text{H}}$ atoms at 400 m/s have a de-Broglie wavelength of about 1 nm. Hence the deflectometry is governed by classical dynamics. The shadow of the beam reproduces the slit positions in the gratings but is vertically shifted according to the free fall of $\overline{\text{H}}$ in the deflectometer. The expected shift of the shadow pattern under the influence of gravity or any other force can be calculated as follows.

The starting conditions for a $\overline{\text{H}}$ atom at the source are given by its vertical position x_0, its vertical velocity component v_0 and the time t it takes for it to cover the distance to the first grating at z_1 (this implies the longitudinal velocity component). The condition for the atom to pass the first grating is that its vertical position at z_1 is inside a slit:

$$x(z_1) \in T_1, \tag{2.5}$$

where T_1 is the set of x values that are in a slit of the first grating. The position at the first grating is given by:

$$x(z_1) = x_0 + v_0 t + \frac{1}{2}at^2 \text{ with } a = \frac{F_\perp}{m_i}. \tag{2.6}$$

Here $F_\perp$ is the vertical force component on the atom and m_i its inertial mass. In analogy to (2.5) and (2.6) the condition to pass the second grating at z_2 after a further time span t is found to be:

$$x(z_2) \in T_2 \tag{2.7}$$

$$x(z_2) = x_0 + v_0 2t + \frac{1}{2}a(2t)^2. \tag{2.8}$$

From (2.6) and (2.8) the following condition for v_0 is obtained:

$$v_0 = \frac{1}{t}(x_2 - x_1) - \frac{3}{2}at. \tag{2.9}$$

After a further time span t the atom will reach the detector. The atom's vertical position at the detector $x(z_3)$ yields:

$$\begin{aligned} x(z_3) &= x_0 + v_0(3t) + \frac{1}{2}a(3t)^2 \\ &= -x_1 + 2x_2 + at^2. \end{aligned} \tag{2.10}$$

For the second equation (2.6) and (2.9) were used. The first two terms on the right hand side of (2.10) show that the shadow on the detector indeed reproduces the periodicity of the slits. Vertical forces on the atom will shift the shadows according to the third

term. [45]

Assuming normal gravity and a grating - grating distance of 40 cm and a velocity distribution like Fig. 3.3 the free fall will be some tens of μm. Therefore the relative vertical position of the grating and the detector must be known very accurately. This is achieved by shining light through the deflectometer which produces an interference pattern (Laué Talbot interferometer) according to the position of the slits (see Fig. 2.6).
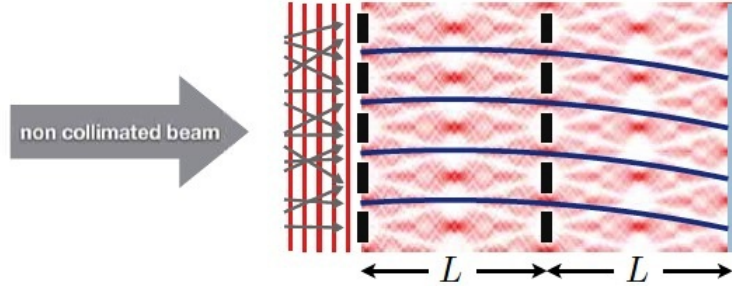

Figure 2.6.: Moiré deflectometer producing a shifted pattern of $\overline{H}$'s on the detector. A light interference pattern is used for position referencing. Taken from [36]

After the experiment the emulsion is removed and analysed by an automated vertex reconstruction system that determines the position of the $\overline{p}$ annihilations on a titanium foil close to the emulsion. It is investigated whether this foil might be replaced by a silicon pixel detector. It will be mainly pions from $\overline{p}$ annihilations that leave visible tracks in the emulsions while the e^+'s will annihilate immediately into 2 γ's that are not used for detection. From the relative position of the annihilations to the light pattern on the emulsion the free fall can be determined only if the velocity of the $\overline{H}$'s is known. As the emulsion does not provide any time information of the annihilations a further time of flight (TOF) detector is required. Scintillating fibres behind the emulsion will be used for this purpose. Knowing the TOF and when the $\overline{H}$ was accelerated (inferred from the time when the electric field for Stark acceleration is turned on) all information is present in order to determine the gravitational acceleration for every detected $\overline{H}$ on the emulsion.

It is estimated that the 1 % level in $\frac{g_{Hbar}}{g}$ should be achievable within months once a temperature as low as 100 mK is reached.

2.4. Hyperfine Spectroscopy with a Rabi-like experiment

As pointed out above the measurement of ground state hyperfine splitting is an additional goal of AEGIS. For this purpose the gravity module which contains the deflectometer and the detectors will be removed. Instead the spectroscopy module will be attached to the down stream side of the 1 T trap. It will contain a sextupole magnet, a tuneable microwave cavity, a superconducting sextupole magnet and finally a $\overline{H}$ detector (see Fig. 2.7). The applied way of measuring the hyperfine splitting with an atomic beam

is known as the Rabi method. Isodor Isaac Rabi proposed this technique in 1938 to measure nuclear magnetic moments.
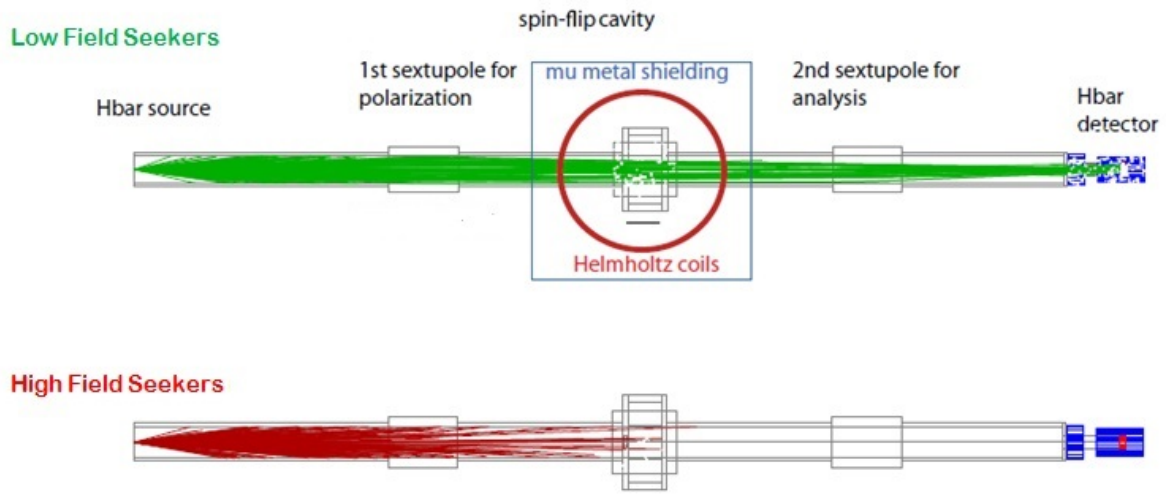

Figure 2.7.: Rabi like experiment with $\overline{\mathrm{H}}$. Trajectories of low field seekers (green) and high field seekers (red) are shown. No transitions are induced in the cavity (off resonance).

The $\overline{\mathrm{H}}$ beam from the 1 T trap will contain all four hyperfine states with roughly equal probability. As shown in Fig. 3.1 two of these states lower their energy level in an external magnetic field (high field seekers, HFS). Therefore these atoms will be defocused by a magnetic sextupole field that has its minimum on the beam axis. For $\overline{\mathrm{H}}$ in one of the other two states (low field seekers, LFS) the opposite is true. Hence a sextupole will separate the $\overline{\mathrm{H}}$'s according to their hyperfine state and focus the LFS (see Section 3.1 for more details).

In the microwave cavity a spin flip transition between a high and a low field seeking state can be induced if the cavity is on resonance with a transition. After the first sextupole the beam contains more LFS than HFS. Therefore the cavity will induce more LFS to HFS transitions than HFS to LFS transitions. As a result the fraction of HFS in the beam is increased in the cavity. Through a subsequent sextupole (second sextupole in Fig. 2.7) these $\overline{\mathrm{H}}$'s will be defocused while the reduced number of LFS is focused towards the $\overline{\mathrm{H}}$ detector. Thus the count rate at the detector is reduced if the cavity is on resonance. Via repetition of the measurement with different frequencies a scan for the transition frequencies can be made. For more details of the spectroscopy measurements see [29, 46].

3. Beam Optics Simulations of an Atomic (Anti-) Hydrogen Beam

As described in Section 2.4 the hyperfine spectroscopy experiment requires a sextupole magnet for separation of high and low field seeking atoms. A sextupole magnet will defocus the high field seekers which will then annihilate on the beam pipe. The low field seekers will be focused and fly towards the cavity. Ideally the first focussing produces a parallel beam of low field seekers and the second one focuses them on the detector. Since the focal length of the sextupole magnet depends on the velocity and hyperfine state of the atoms complete focussing can not be achieved. Therefore simulations are used to figure out what the ideal sextupole configuration is.

For the gravity experiment a sextupole is not necessary. However, if its focusing effect on the low field seeking atoms overcompensates the loss of high field seekers, which will be roughly 50 %, a permanent implementation of a sextupole in the AEGIS beam line should be considered.

Before discussing the beam optics simulations the underlying magnetic properties of (anti-) hydrogen atoms are outlined in the following section.

3.1. Magnetic Properties of Ground State Hydrogen

Transport of ground state $\overline{\mathrm{H}}$ through a magnetic field is governed by the Zeeman effect on the hyperfine states. To investigate this theoretically time independent perturbation is applied in first order to the analogous problem in hydrogen. The following calculation is based on [47]. Necessary calculations omitted it this paper are provided in Appendix A. Hyperfine splitting of the 1s ground state arises from the interaction of the e^- spin ($\mathbf{S}$) and the proton spin ($\mathbf{I}$). Additionally the Zeeman effect is introduced by the interaction of $\mathbf{S}$ and $\mathbf{I}$ with the external magnetic field $\mathbf{B} = (0, 0, B)$. The Hamiltonian associated with these interactions is given by:

$$H_{HFS} = A\,\mathbf{IS} + (aS_z + bI_z)B. \tag{3.1}$$

A is the hyperfine coupling constant which is experimentally determined to be approx. 1.42 GHz $\times$ h $\simeq$ 5.9 μeV. b is the abbreviation for $-g_N\mu_N$. The proton's g-factor is given by $g_N \simeq 5.6$. The nuclear magneton $\mu_N = \frac{e\hbar}{2m_P}$ is defined in terms of the proton mass m_P and the elementary charge e. The negative sign in the definition of b results from the different sign of the proton charge with respect to the e^- charge. a is the analogue expression for the e^-: $g_S\mu_B$. For convenience angular momenta in this section are expressed in the unit of $\hbar$.

As shown in Appendix A H_{HFS} commutes with z-component F_z of the total angular moment $\mathbf{F} = \mathbf{I} + \mathbf{S}$. Therefore the eigenstates of F_z are also eigenstates of H_{HFS}. It is notable that for $B \neq 0$ the magnitude of the total angular momentum is not conserved: $[H_{HFS}, F^2] \neq 0$ (see Appendix A).

For the calculation of eigenenergies and eigenstates of H_{HFS} it is convenient to introduce the usual ladder operators $I_\pm = I_x \pm i I_y$ and $S_\pm = S_x \pm i S_y$. Using these operators H_{HFS} can be written as:

$$H_{HFS} = A\, I_z S_z + \frac{A}{2}(S_+ I_- + S_- I_+) + (a S_z + b I_z)B. \tag{3.2}$$

In order to obtain the matrix elements of H_{HFS} the basis of $|m_S, m_I\rangle = |S, m_S\rangle\,|I, m_I\rangle$ is used. Here $S = I = \frac{1}{2}$ are the e$^-$ and proton spin. The matrix elements are found to be:

$$\langle m_{S'}, m_{I'}|\, H_{HFS} \,|m_S, m_I\rangle = \Big(A m_S m_I + m_S a B + m_I b B\Big)\delta_{m_{S'},m_S}\delta_{m_{I'},m_I} +$$
$$\frac{A}{2}\sqrt{(S-m_S)(S+m_S+1)(I+m_I)(I-m_I+1)}\delta_{m_{S'},m_S+1}\delta_{m_{I'},m_I-1} + \tag{3.3}$$
$$\frac{A}{2}\sqrt{(S+m_S)(S-m_S+1)(I-m_I)(I+m_I+1)}\delta_{m_{S'},m_S-1}\delta_{m_{I'},m_I+1},$$

The first term gives diagonal elements and can be obtained directly from the first and third term in (3.2). The other terms are obtained using that the action of a general angular momentum ladder operator $J_\pm = J_x \pm i J_y$ on the states $|J, m_J\rangle$ (eigenstates of J^2 and J_z) is given by:[1]

$$J_\pm\,|J, m_J\rangle = \sqrt{j(j+1) - m_J(m_J \pm 1)}\,|J, m_J \pm 1\rangle =$$
$$\sqrt{J^2 + J - m_j^2 \mp 1}\,|J, m_J \pm 1\rangle = \sqrt{(J \mp m_J)(J \pm m_J + 1)}\,|J, m_J \pm 1\rangle. \tag{3.4}$$

For a ground state hydrogen atom an ordered basis of $|m_S, m_I\rangle$ is given by: $|\frac{1}{2}, \frac{1}{2}\rangle, |\frac{1}{2}, -\frac{1}{2}\rangle,$ $|-\frac{1}{2}, \frac{1}{2}\rangle, |-\frac{1}{2}, -\frac{1}{2}\rangle$. In this basis H_{HFS} takes the form:

$$H_{HFS} = \frac{1}{4}\begin{pmatrix} A + 2B(a+b) & 0 & 0 & 0 \\ 0 & -A + 2B(a-b) & 2A & 0 \\ 0 & 2A & -A - 2B(a-b) & 0 \\ 0 & 0 & 0 & A - 2B(a+b) \end{pmatrix}.$$
$$\tag{3.5}$$

Hence for states with $m = m_S + m_I = \pm 1$ the matrix is diagonal and therefore the states $|\pm\frac{1}{2}, \pm\frac{1}{2}\rangle$ are eigenstates with the energies:

$$E_{m=\pm 1} = \frac{A}{4} \pm \frac{(a+b)B}{2}. \tag{3.6}$$

---

[1] For a derivation see standard Quantum Mechanics textbooks like [48] Chapter 6.

The 2×2 matrix of the two states with $m = 0$ has four non-zero components. The eigenenergies are:

$$E_{m=0}^{\pm} = -\frac{A}{4} \pm \frac{1}{2}\sqrt{(a-b)^2 B^2 + A^2}. \tag{3.7}$$

By comparison of (3.6) and (3.7) it is found that the hyperfine splitting in zero field ($B = 0$) is A and that the higher energy level has threefold degeneracy. Eigenvectors corresponding to the eigenenergies $E_{m=0}^{\pm}$ are calculated in Appendix A. The result is:

$$\begin{aligned}
|E_{m=0}^{+}\rangle &= \cos\left(\frac{\alpha}{2}\right)\left|\frac{1}{2}, -\frac{1}{2}\right\rangle + \sin\left(\frac{\alpha}{2}\right)\left|-\frac{1}{2}, \frac{1}{2}\right\rangle \\
|E_{m=0}^{-}\rangle &= -\sin\left(\frac{\alpha}{2}\right)\left|\frac{1}{2}, -\frac{1}{2}\right\rangle + \cos\left(\frac{\alpha}{2}\right)\left|-\frac{1}{2}, \frac{1}{2}\right\rangle,
\end{aligned} \tag{3.8}$$

with α defined by $\tan(\alpha) = \frac{A}{(a-b)B}$. Only in zero field $\alpha = \frac{\pi}{2}$ and the states $|E_{m=0}^{+}\rangle$ and $|E_{m=0}^{-}\rangle$ become a triplet ($F = 1$, $m = 0$) and singlet ($F = 0$, $m = 0$) eigenstate of $\mathbf{F}^2$:[2]

$$|E_{m=0}^{\pm}\rangle = \frac{1}{\sqrt{2}}\left(\pm\left|\frac{1}{2}, -\frac{1}{2}\right\rangle + \left|-\frac{1}{2}, \frac{1}{2}\right\rangle\right). \tag{3.9}$$

In general the $m = 0$ states are composed of a triplet and singlet component. For a large B field $\alpha \to 0$ and the eigenstates become:

$$\begin{aligned}
|E_{m=0}^{+}\rangle &= \left|\frac{1}{2}, -\frac{1}{2}\right\rangle \\
|E_{m=0}^{-}\rangle &= \left|-\frac{1}{2}, \frac{1}{2}\right\rangle,
\end{aligned} \tag{3.10}$$

which are eigenstates of $\mathbf{S}^2$ and $\mathbf{I}^2$ but not of $\mathbf{F}^2$.[3]

Using $\mu = -\dfrac{\partial E}{\partial B}$ the magnetic moments of the four hyperfine states can be determined to be

$$\begin{aligned}
\mu_{m=\pm 1} &= \mp\frac{1}{2}(a+b) \approx \mp\frac{1}{2}g_S\mu_B \approx \mp\mu_B \\
\mu_{m=0}^{\pm} &= \mp\frac{1}{2}\frac{(a-b)^2 B}{\sqrt{(a-b)^2 B^2 + A^2}} \approx \mp\frac{x\mu_B}{\sqrt{x^2+1}}, \text{ with } x = \frac{2\mu_B B}{A}.
\end{aligned} \tag{3.11}$$

Energies and magnetic momenta of the four hyperfine states are shown in Fig. 3.1. For sufficiently large B (> 0.1 T) the magnetic behaviour is governed by the e$^-$ spin since the associated magnetic moment is about 660 times larger in magnitude than the proton's. Summarizing the previous considerations, it was found that m_S, m_I are exact quantum numbers for $B \to \infty$ and F, m for $B \to 0$.

---

[2]For details see Chapter 10.2.3 and 12.5.4 of [48].

[3]This is in accordance with the previous result: $[H_{HFS}, F^2] \neq 0$

If a hydrogen atom passes through a magnetic field that varies sufficiently slowly in the atom's rest frame its magnetic moment will stay parallel to the B field and the magnetic energy can be expressed in terms of the magnitudes of $\boldsymbol{\mu}$ and $\mathbf{B}$: $E = -\boldsymbol{\mu}\mathbf{B} = -\mu B$. This is the case if the relative change of the B field per unit time is much less than the Larmor frequency ω_L of the relevant magnetic dipole transitions: [27] [49]

$$\frac{1}{B}\frac{dB}{dt} \ll \omega_L. \tag{3.12}$$

Since the experiment requires separation of low and high field seekers the transitions between $F = 1 \leftrightarrow F = 0$ (see Fig. 3.1) should not be induced by a B field gradient in the beam line.
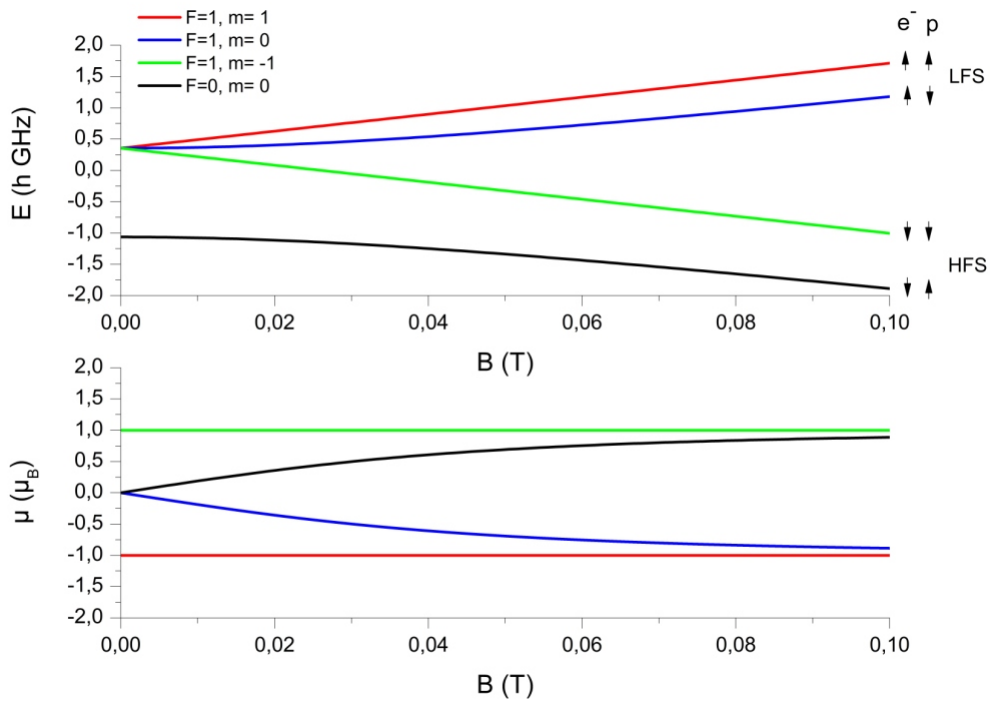

Figure 3.1.: Energy levels (top) and magnetic moments (bottom) of the hyperfine states in hydrogen. The Zeeman effect splits the triplet state. States that increase/decrease their energy in a B field are indicated as LFS/HFS (Low/High Field Seekers). In strong magnetic fields the e$^-$ and proton spins decouple and the shown spin configuration results.

For a sextupole field $B = cr^2$, where r is the radial coordinate and c is a constant. A sextupole field in the plane normal to the beam direction and constant along this direction will exert the following radial force on the atoms:

$$F_r = -\frac{\partial E}{\partial r} = -\frac{\partial E}{\partial B}\frac{\partial B}{\partial r} = \mu(B)2cr. \tag{3.13}$$

$\mu(B)$ depends on the state of the atom according to (3.11). For the low field seeking $m = 1$ state this force is harmonic and leads to a sinusoidal trajectory. The high field seeking $m = -1$ state is defocused and follows a hyperbolic trajectory. The trajectories of the $m = 0$ states are more difficult to determine since here μ depends on B (see (3.11)). The simulations study B Fields up to about 2 T and hence μ can not be approximated to be constant for the $m = 0$ states (see Fig. 3.1).

These results were obtained for hydrogen. In the simulations of the $\overline{\text{H}}$ beam CPT symmetry is assumed. Therefore the charges of the e^- and the proton have to switch their signs and the energy levels would be identical to what was calculated for hydrogen. The only difference is that for $\overline{\text{H}}$ the spins of the e^+ and $\overline{p}$ will be antiparallel to the corresponding spins of their antiparticles in hydrogen (Fig. 3.1).

A simple estimation for the focal length l_F of a sextupole magnet can be obtained by assuming that μ is constant: $\mu = -\mu_B$. In this case the frequency ω of the oscillations of the LFS in a sextupole field is given by (3.13). Then l_F can be calculated as one fourth $\left(\frac{\pi}{2}\right)$ of an oscillation:

$$\omega = \sqrt{\frac{2c\mu_B}{m}} \rightarrow l_F = \frac{\pi}{2\omega}v_z = \frac{\pi}{2}v_z\sqrt{\frac{m}{2c\mu_B}} = \frac{\pi}{2}v_z r_1\sqrt{\frac{m}{2\mu B_1}}. \tag{3.14}$$

For the last equation $c = \frac{B_1}{r_1^2}$ was used, where B_1 is the pole field strength and r_1 the inner radius of the sextupole. The following plot shows l_F calculated for different values of the horizontal velocity v_z:
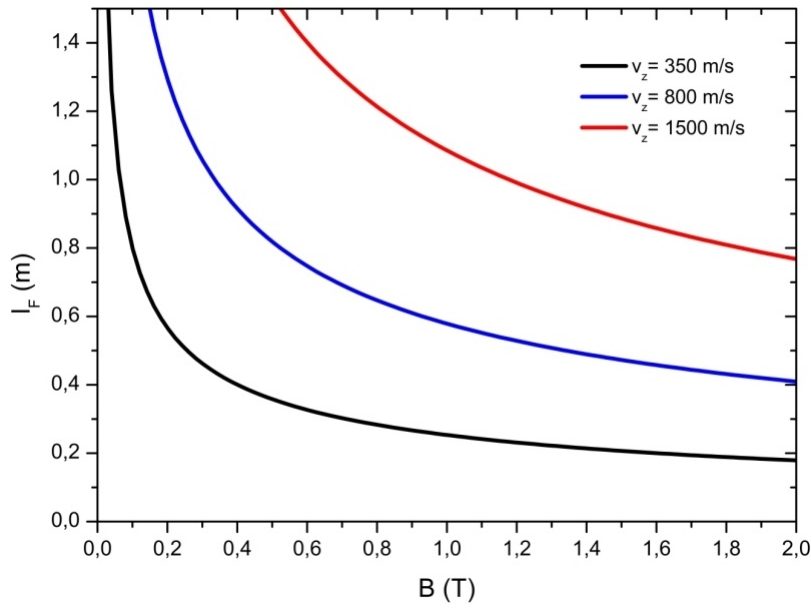

Figure 3.2.: Focal length l_F in dependence of pole field strength B for different horizontal velocities v_z. r_1 was set to 5 cm, which is the value that will be used in the simulations.

3.2. Simulations

The passage of $\overline{H}$ atoms through a magnetic sextupole field was simulated using the GEANT4 Toolkit [50]. GEANT4 is mainly used in high energy physics and medical physics. It allows to track particles in user defined fields and to simulate their interactions with materials. GEANT4 simulation codes are written in C++.

The user can precisely define geometries and materials of the experimental setup. For the purpose of this work only particle tracking in magnetic sextupole fields is relevant. The detectors of the gravity and HFS experiment were assumed to be ideal. While the HFS detector only counts arriving $\overline{H}$'s the gravity detector also records their position. In both cases the simulated data is written to a ROOT file[4]. Additionally the coordinates of annihilations of $\overline{H}$'s on surrounding beam pipes are saved in these files. This will allow to determine where $\overline{H}$'s are lost in the beam line (see Fig. 3.8).

As GEANT4 is mainly used in particle physics it does not have bound particles like $\overline{H}$ in its libraries. Therefore it was necessary to implement a new particle type with the properties expected from $\overline{H}$ atoms. This was done by members of the Stefan-Meyer Institute and their collaborators in the ASACUSA experiment [52]. The simulation program I started to work with was able to do simulations of the trajectories of $\overline{H}$'s in a given hyperfine state under the conditions of the ASACUSA experiment. The task was to modify the existing simulation with several hundred pages of C++ code in order to allow simulations with the geometry and beam parameters of AEGIS. It was for instance necessary to implement the possibility to determine the velocity of the antihydrogen atoms according to a given probability distribution (Fig. 3.3). Additionally the construction of the periodic grating structure had to be added. Simulation parameters in the program are controlled conveniently with user defined commands in a macro file. By modifying these macro files the simulation geometry was changed to be suitable for AEGIS. Python scripts were used to produce macro files with the desired parameters (e.g. temperature, B fields) automatically. These macro files were then consecutively executed and ran the simulations. Further macros (C++) were written and used to extract the relevant data from the ROOT files and to allow analysis and visualization.

The starting conditions of $\overline{H}$'s are provided by an assumed probability distribution for their position and their velocity. The initial position is chosen according to the $\overline{p}$ cloud in the trap. In the simulation this distribution is assumed to be Gaussian with a longitudinal FWHM of 8 mm and a transversal FWHM of 1.5 mm. The Maxwell-Boltzmann distribution provides the velocities for a given temperature. In addition an axial velocity component (Stark acceleration) according to the green curve in Fig. 3.3 is added. It should be kept in mind that in the real experiment only 50 % of $\overline{H}$'s will be accelerated in the right direction (see Section 2.2.3). $\overline{H}$'s in the simulations are assumed to be in their ground state.

For the numerical integration of the equation of motion the fourth order Runge-Kutta method was used. The maximum allowed step size was chosen to be 1 cm. GEANT4

---

[4]ROOT is an object orientated framework for the analysis and visualization of large amounts of data. [51]

uses adaptive step size control that tries to maximize the step lengths while maintaining the required precision of the trajectory. This reduces the number of required steps in the simulation and makes them more time efficient. The adaptive step size routine[5] ensures
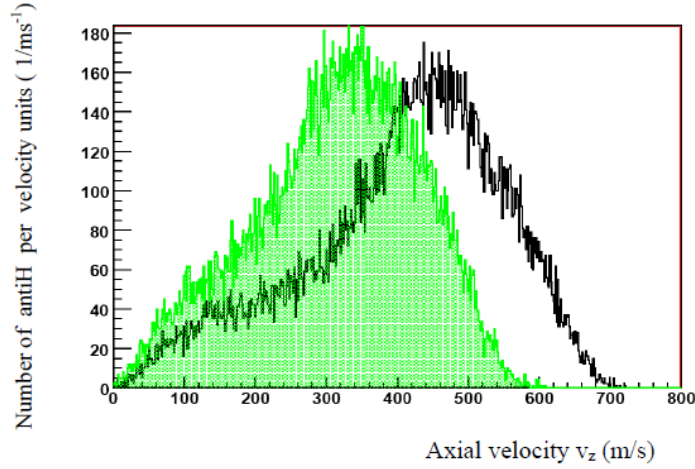

Figure 3.3.: Simulated axial velocity distribution due to Stark acceleration for 100 mK $\overline{\mathrm{p}}$ temperature. The black curve shows the result without the effect of the 1 T field and the green one with the 1 T field. Taken from [43]

that the step size $|\mathbf{x}|$ is maximized under the condition that the relative error in space and momentum propagation is within the default bounds of:

$$0.5 \times 10^{-7} < \frac{|\Delta\mathbf{x}|}{|\mathbf{x}|}, \frac{|\Delta\mathbf{p}|}{|\mathbf{p}|} < 0.05. \tag{3.15}$$

The algorithm applied for that is similar to what is found in chapter 17.2. of [53]. Results obtained with 1 cm maximum step size could be reproduced with a maximum step size of 10 μm, which is certainly small enough. This suggested that 1 cm is precise enough as well.

3.2.1. Sextupole in the HFS Setup

The first simulations examined the influence of the following parameters on the count rate of the HFS experiment:

- $\overline{\mathrm{H}}$ temperature T

- Distance d between $\overline{\mathrm{H}}$ source and first sextupole

- Pole field strengths B_1 and B_2 of the first and second sextupole.

---

[5]More details found in the Geant4 online documentation: `http://geant4.cern.ch/support/source/geant4/source/geometry/magneticfield/include/G4MagIntegratorDriver.hh`.

The geometry of the simulation and a technical drawing of the 1 T trap (see Fig. 2.4 middle) are depicted in Fig. 3.4. The position of the source in the axial 1 T field of the Penning trap and the corresponding position in the simulation geometry are indicated. Trajectories of $\overline{H}$ atoms are shown by red/green lines for high/low field seekers.

$\overline{H}$'s will leave the source towards the right hand side and pass through the first sextupole magnet. The source - sextupole distance d was simulated with 25, 55 and 120 cm. In each case the sextupole field length was 10 cm. As indicated by the dashed blue lines in Fig. 3.4 the shorter two distances (25 cm and 55 cm) would correspond to a sextupole magnet that is inside the cold 1 T formation trap. A gate valve at the end of the 1 T vacuum chamber will act as an interface between the 1 T trap and the attached experiment. This would allow to detach the experiments (gravity and spectroscopy) and exchange them without breaking the vacuum and warming up the superconducting magnets of the trap. This gate valve would be located behind the positions of the sextupole at 25 and 55 cm. As a result the magnets would not have to be removed when experiments are changed. Since the design of the interface is not yet finalized a place holder for it was included in Fig. 3.4.

After that the $\overline{H}$'s pass through the afore mentioned interface and enter the spectroscopy module. In the case of $d = 120$ cm the $\overline{H}$'s would pass through the sextupole field at this position.

Distance from Source (cm)	Diameter of Aperture (cm)	Element
25-35, 55-65, 120-130	10	1st Sextupole
158-200	10	RF - Cavity
224-246	10	2nd Sextupole
315	4	Detector

Table 3.1.: Dimensions of the HFS beam line.

Next the $\overline{H}$'s enter the radio frequency spin flip cavity where the hyperfine transition can be induced. For the simulations the cavity was turned off. The cavity is surrounded by two Helmholtz coils (yellow in Fig. 3.4) that will produce a certain background B field in the cavity. This field is negligibly weak and therefore not simulated.

The following second sextupole will focus $\overline{H}$'s towards the detector. This magnet is superconducting (fields up to 3.5 T) and has a field length of 22 cm.

Finally the $\overline{H}$'s will hit the detector (inside orange region in Fig. 3.4) where the count rate is recorded. For the diameter and the position of beam line elements along the beam line see Table 3.1.
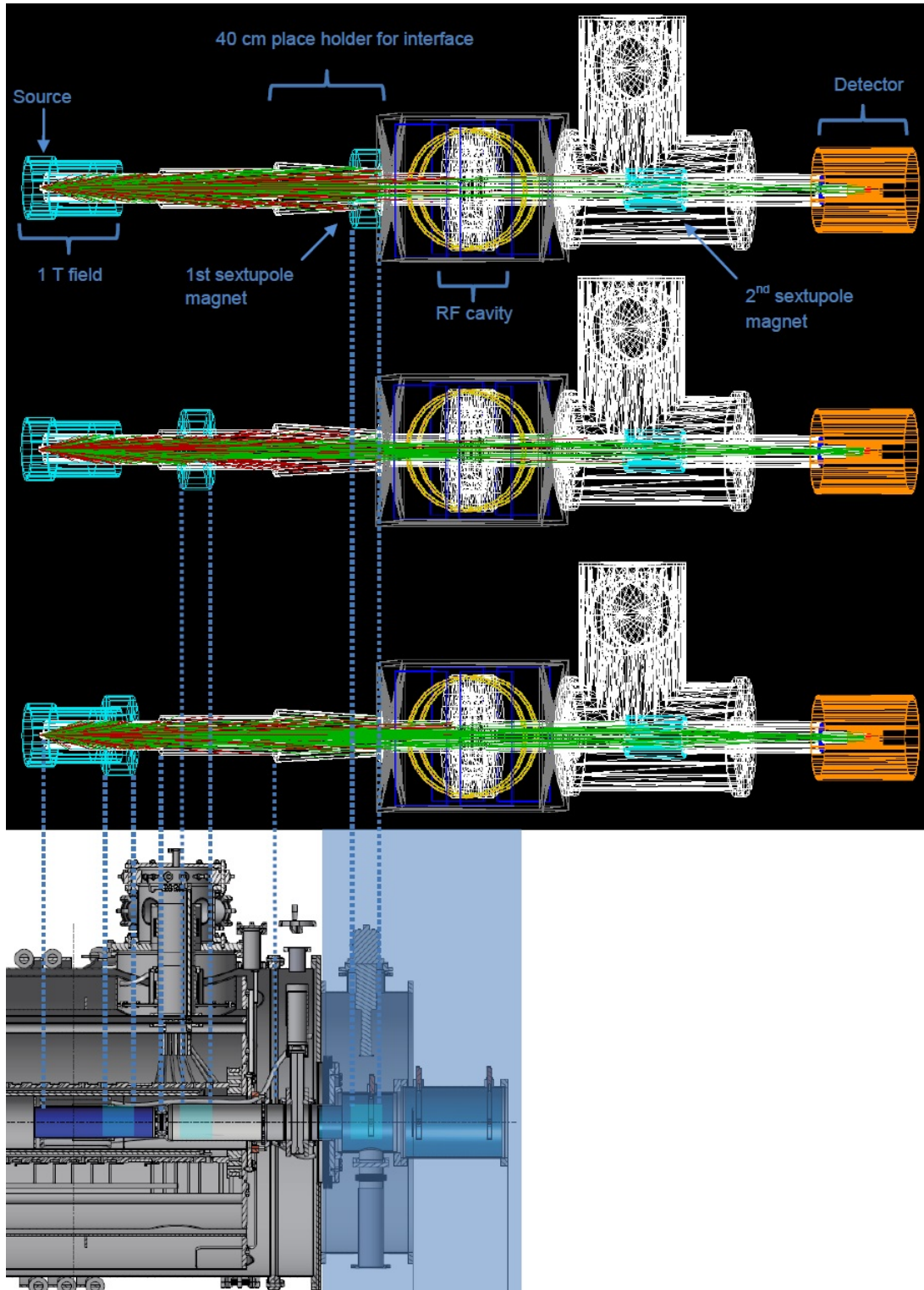
Figure 3.4.: First three rows show the simulation geometry for the HFS setup. From top to bottom the source - sextupole distances are 120, 55, 25 cm. In the last row a technical drawing of the 1 T magnet is shown. Magnetic field in the simulation geometry is shown as a blue volume. In the blue shadow the gravity module is visible at the position were the spectroscopy module would be attached.

Exemplarily some results of the simulations are plotted in Fig. 3.5. The colour indicates the simulated number of counts with the field strengths of the first (B_1) and second (B_2) sextupole on the axes. Per pair of B_1 and B_2 10^5 trajectories of $\overline{\mathrm{H}}$'s were simulated and the count rate at the detector was recorded. The increment of the field strengths was 0.1 T. For reasonable efficiencies the obtained number of counts at the detector (n) is large compared to the statistical fluctuation due to shot noise ($\sqrt{n}$). This is necessary to obtain statistically significant simulation results.
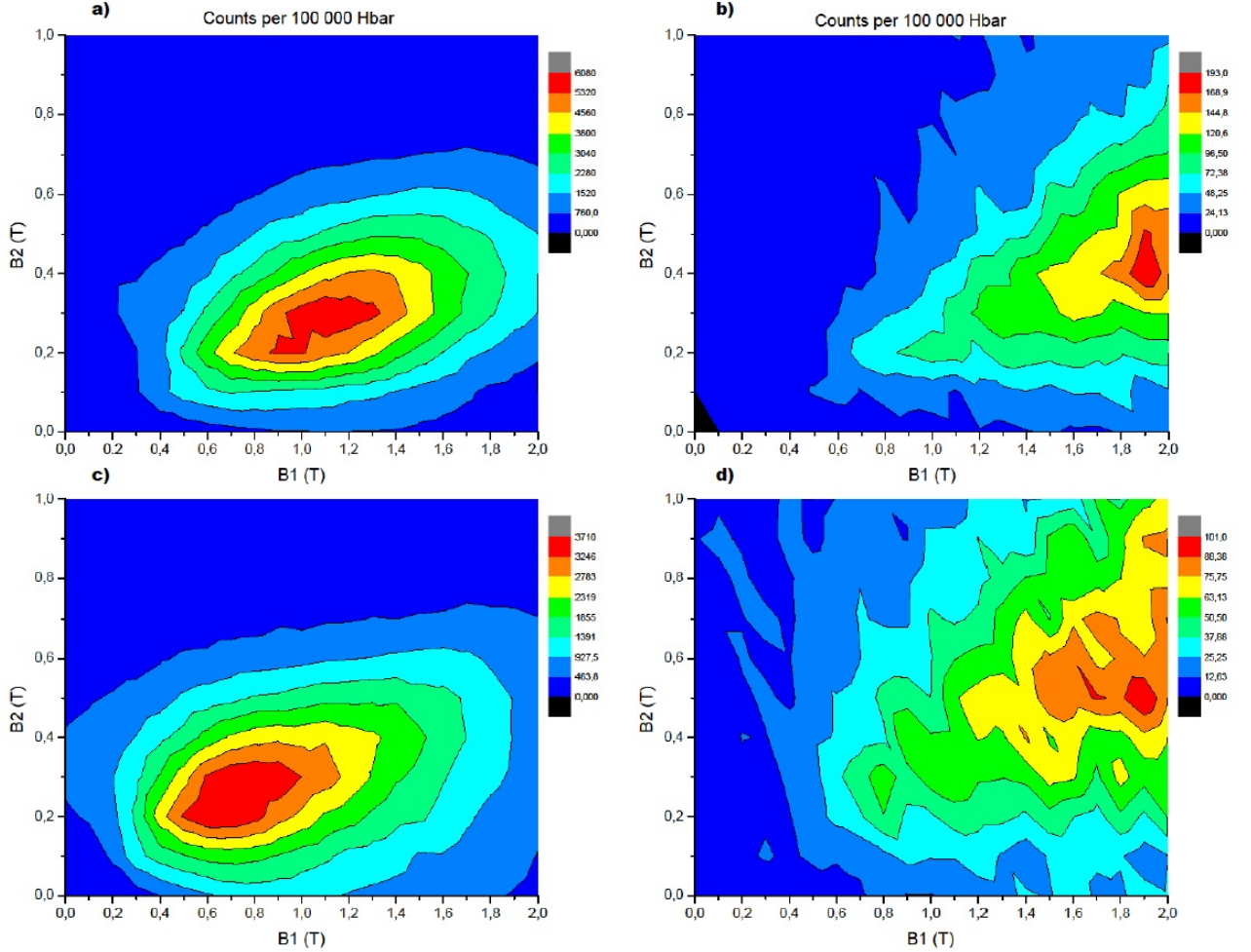

Figure 3.5.: Number of counts per 100 000 $\overline{\mathrm{H}}$'s in dependence of the field strengths of the sextupole magnets. The four plots belong to simulations with differing values for $\overline{\mathrm{H}}$ temperature and distance of the first sextupole from the source: a) 0.1 K, 25 cm b) 7 K, 25 cm c) 0.1 K, 55 cm d) 7 K, 55 cm.

Fig. 3.5 and Table 3.2 show that a smaller d leads to a higher count rate. This is expected as the available solid angle for $\overline{\mathrm{H}}$'s to reach the first sextupole is larger in these cases, which reduces loss on the beam pipes.

Fig. 3.5 shows that for $T = 0.1$ K there are well defined optimal ranges for B_1 and B_2. The same holds for $T = 1$ K (not shown). The shape of the areas with equal number of counts is not isotropic in the B_1 - B_2 plane. For B_1 higher than the ideal value the number of counts drops comparably slowly. This is true especially for directions where B_2 rises slowly with B_1. An explanation for this is that over focusing at the first sextupole (high B_1) leads to more beam divergence at the second sextupole. Therefore higher B_1 requires stronger focusing at the second magnet which means a higher B_2.

This reasoning could also be applied to under focusing at the first magnet. In this case a higher B_2 should compensate for a too low B_1. Hence the areas of equal number in counts should rise in B_2 with B_1 decreasing below its ideal value. This is not observed in Fig. 3.5. An over focused $\overline{\text{H}}$ beam crosses the beam line before it diverges from its focal point onwards while an under focused beam diverges all the way and hits the beam pipe. Hence under focusing is more problematic than over focusing in terms of count rate.

The ideal values for the field strengths according to the simulations can be found in Table 3.2. For $d = 25$ cm the beam is more divergent when it enters the sextupole than in cases of $d = 55$ or $d = 120$ cm. Therefore the ideal value for B_1 is lower in the latter cases.

T (K)	d (cm)	B_1(T)	B_2(T)	Counts
0.1	25	1.1	0.3	6065
1	25	1.6	0.4	1132
7	25	1.9	0.4	193
20	25	2.0	0.5	72
50	25	2.0	0.5	23
0.1	55	0.6	0.2	3709
1	55	1.0	0.3	479
7	55	1.9	0.5	101
20	55	2.0	0.6	47
50	55	1.8	0.8	18
0.1	120	0.3	0.2	2301
1	120	0.4	0.3	230

Table 3.2.: Ideal field strengths (in the range of 0 - 2 T) and number of counts per 10^5 $\overline{\text{H}}$'s in dependence of temperature (T) and the distance within the source and the first sextupole (d).

For the temperature of 0.1 K a typical horizontal velocity that results from Stark acceleration (Fig. 3.3) and the thermal energy (Table 3.3) is 350 m/s. According to Fig. 3.2 a focal length of 25 cm at that velocity corresponds to $B_1 = 1$ T. The simulation suggests an ideal value of $B_1 = 1.1$ T. That the simulated ideal B_1 value is lower can be expected because in the simulation the $\overline{\text{H}}$'s are only for a length of 10 cm in the harmonic potential of the sextupole magnet, which is much shorter than the focal length. The results in Fig. 3.2 are based on the assumption that the $\overline{\text{H}}$'s can make a complete $\pi/2$ oscillation

in the sextupole field, which is not valid in the simulations.

For $d = 55$ and $d = 120$ cm the difference between the values found in Fig. 3.2 and in Table 3.2 are larger because here the sextupole field length in the simulation is even smaller compared to the required focal length.

T (K)	v_{Th} (m/s)
0.1	51
1	161
7	426
20	719
50	1137

Table 3.3.: Velocity of $\overline{\text{H}}$'s according to their temperature.

In case of $T = 1$ K similar observations are made. For higher T the optimal field strengths are out of the simulated range 0 T $< B_{1,2} <$ 2 T. This can be seen for instance in Fig. 3.7 c), where fields up to 5 T were simulated for 7 K in the gravity experiment. As can be seen in Table 3.2 B_2 increases with the temperature in a similar way as B_1. Here the ideal focal length is determined by the distance within the second sextupole and the detector, which is about 90 cm.

The results in Table 3.2 suggest that having the sextupole inside the 1 T trap would lead to a considerable gain in count rate for the spectroscopy experiment. For 0.1 K the short distance $d = 25$ cm leads to 2.6 times higher count rate than $d = 120$ cm. In this case the sextupole would also influence the $\overline{\text{H}}$ beam if the gravity module is attached. Therefore it shall be next investigated whether the sextupoles inside the trap are beneficial the gravity experiment.

3.2.2. Sextupole in the Gravity Setup

The simulations are in principle very similar to the one for the spectroscopy experiment. The difference is the experimental module after the interface (see Fig. 3.6). Now two gratings are in the beam line followed by a position sensitive detector (see Fig. 2.2).

The results should show whether the gain through focusing the LFS exceeds the loss due to defocusing the HFS. Regarding the sensitivity of the gravity measurements any sextupole magnet should be as close as possible to the source in order to ensure that its stray fields do not influence the $\overline{\text{H}}$ free fall in the deflectometer.

Table 3.4 shows the positions of the beam line elements in the gravity experiment. The grating area is 10×10 cm^2. Their thickness is 100 μm, the periodicity 40 μm and the slit width 10 μm. These dimensions are based on assumptions about the final design, which is not yet fixed. The detector was taken to be one meter in diameter to ensure that every $\overline{\text{H}}$ that passes the second grating is detected.

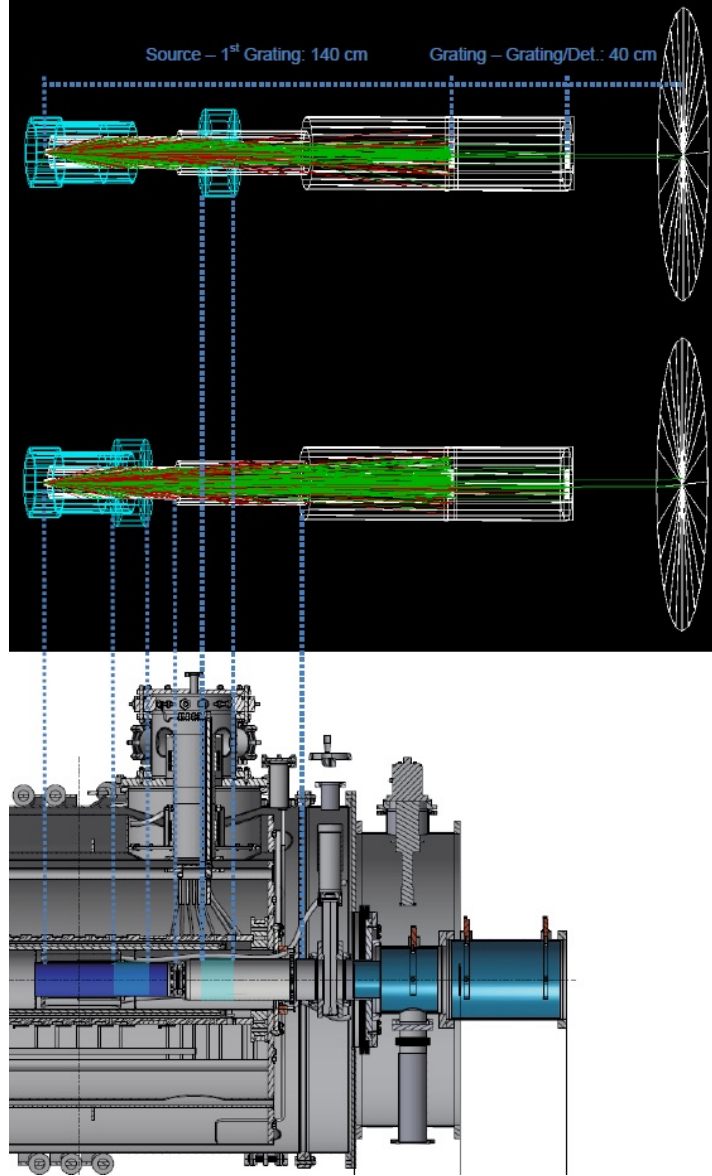| Distance from Source (cm)	Aperture	Element
25-35, 55-65	10 cm diam.	Sextupole
140	10×10 cm^2	1st Grating
180	10×10 cm^2	2nd Grating
220	100 cm diam.	Detector

Table 3.4.: Dimensions of the gravity beam line.

Figure 3.6.: First two rows show the simulation geometry for the gravity experiment with $d = 25$ cm and $d = 55$ cm. The positions of the sextupole fields are shown in blue and are indicated in a technical drawing of the 1 T trap (bottom). Green trajectories belong to LFS, red ones to HFS.

For thechnical reasons the real detector is foreseen to be much smaller, about 10×10 cm^2. The impact of the size limitation of the sensitive detector area is addressed in Section 3.2.3.

In case of the gravity experiment not only the number of counts is recorded but also the position on the detector.

Trajectories of 100 000 $\overline{\mathrm{H}}$'s were simulated for each value of the sextupole field strength B. The increment of B was 0.1 T.
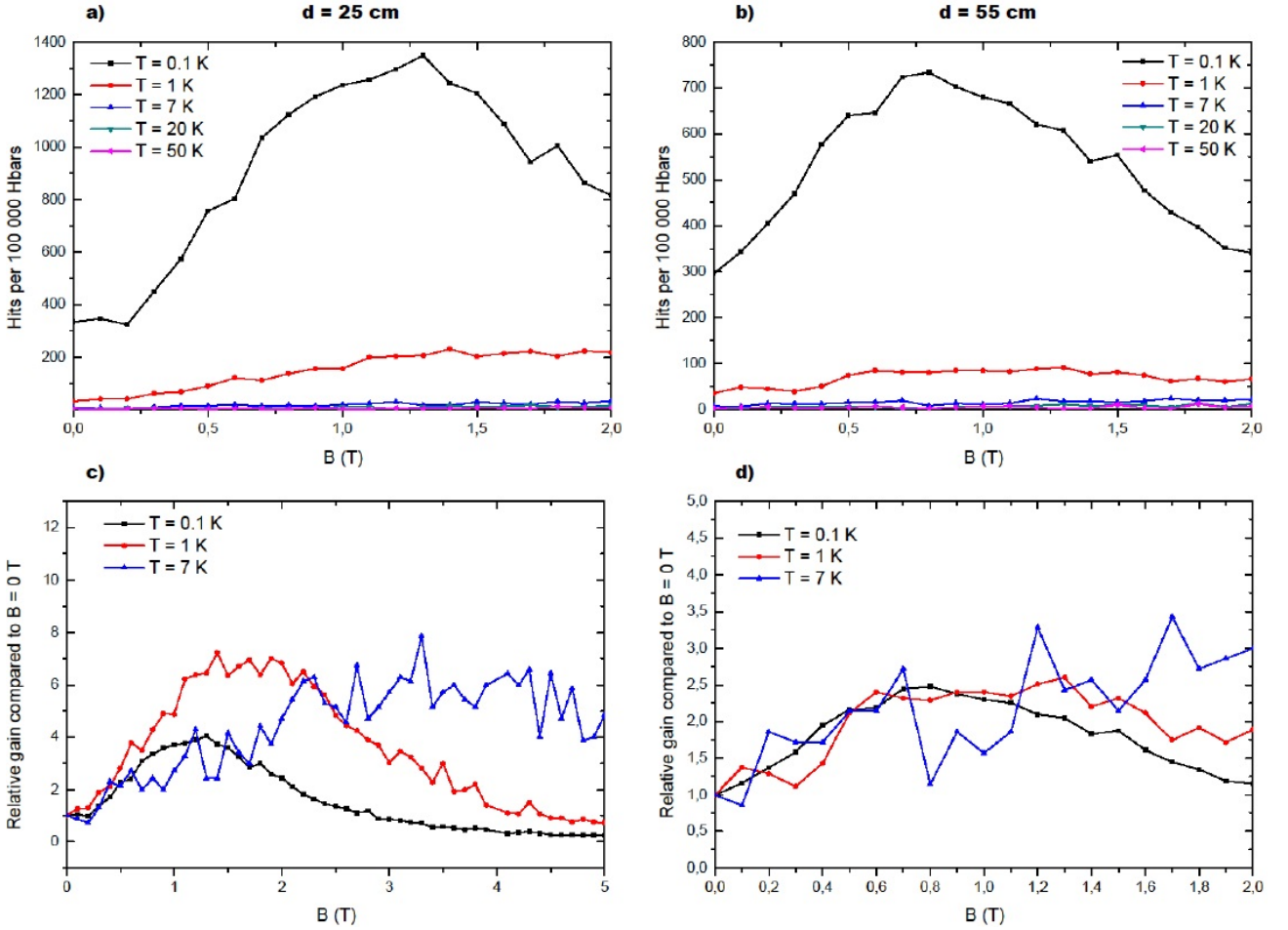

Figure 3.7.: The number of counts per 100 000 $\overline{\mathrm{H}}$'s in the gravity experiment is shown in a) with the sextupole at $d = 25$ cm and in b) with $d = 55$. c) ($d = 25$) and d) ($d = 55$) show the relative gain in counts $\frac{n(B)}{n(B)|_{B=0\mathrm{T}}}$, that is attainable by the implementation of a sextupole magnet.

Fig. 3.7 shows that a sextupole can increase the count rate for the gravity experiment. For given values of d and T the ideal field strengths B in the gravity experiment match roughly those obtained for B_1 in the spectroscopy experiment (compare Fig. 3.7 and Table 3.2). This is expected as for both experiments the sextupole after the source

reduces the beam divergence as much as possible in the ideal case. Fig. 3.7 shows that a too small B causes a more severe reduction in counts than a higher B. This is best visible in the curves for $T = 0.1$ and 1 K in graph c). A similar tendency was found in the spectroscopy results.

Also the relative drop in count rate with rising temperature is comparable in the simulations of the gravity and spectroscopy experiment (see Table 3.2 and Fig. 3.7).
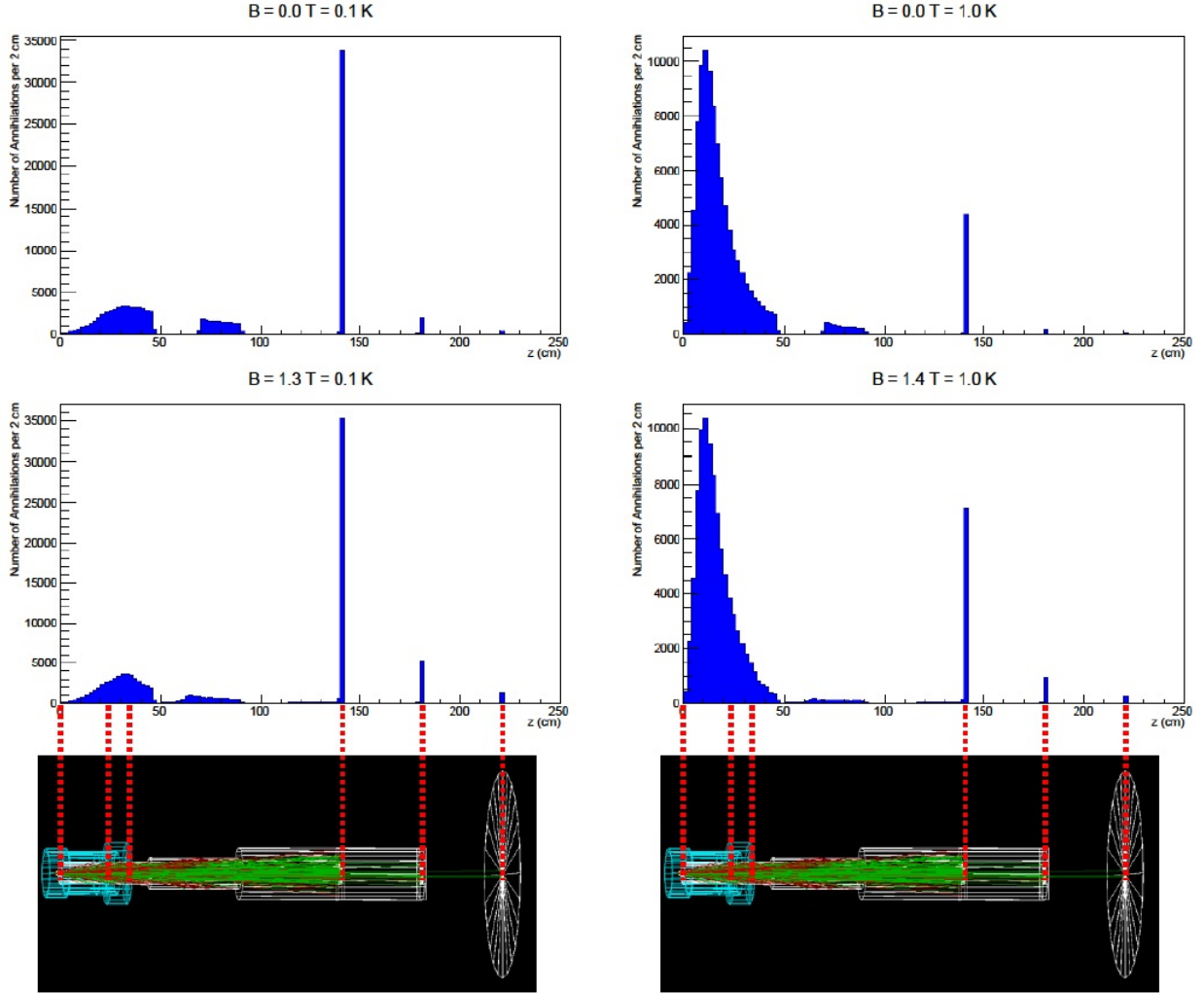

Figure 3.8.: The number of annihilations along the beam line is shown for $d = 25$ cm and the temperatures 0.1 K and 1.0 K. The binning size is 2 cm. The cases with no sextupole field and the ideal field strengths for the two temperatures are shown. Please note the different scales of the y-axes.

In graph c) of Fig. 3.7 it is visible that the ideal field strength rises with temperature and hence with the velocity, which is expected. That the relative gain also rises with tem-

perature requires further considerations. The gain achieved through the magnet results from its focusing, which reduces annihilations on the beam pipes. The second reason for loss are annihilations on the gratings. From the histograms in Fig. 3.8 it can be seen that for higher temperatures the ratio of wall annihilations to grating annihilations is larger. This is expected since in this case the beam is more divergent. Thus also the relative fraction that is "saved" by the magnet is larger. For ideal focusing (lower two histograms in Fig. 3.8) the number of wall annihilations is reduced after the sextupole and more $\overline{H}$'s reach the gratings and the detector.

For $d = 55$ cm (Graph b) and d) in Fig. 3.7) the number of counts is lower. This is because the sextupole magnet can only reduce annihilation behind the magnet, hence also the relative gain is lower. In comparison to $d = 25$ cm the ideal field strengths are lower for $d = 55$ cm because after a larger distance the beam is less divergent.
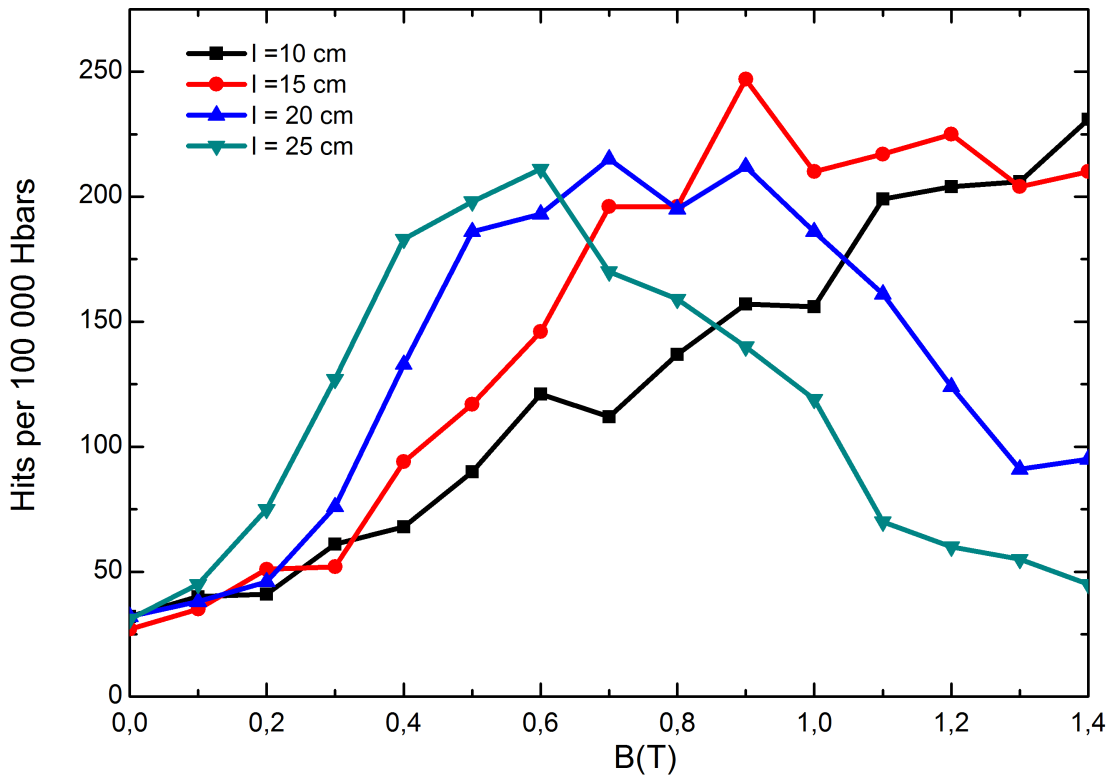

Figure 3.9.: Number of counts in the gravity experiments for $d = 25$ cm and 1 K. Increasing the sextupole field length l results in a reduction of the ideal field strength.

In general the ideal field strength will grow with lower d and higher temperature. From the considerations in the previous paragraph it follows that d should be minimized as far as technically possible. Since usage of a permanent sextupole magnet would limit the field strengths to about 1.4 T the field strength may become a limiting factor for

the efficiency. Fig. 3.7 shows for example that with $d = 25$ cm the ideal field strength for temperatures of 1 K and higher is above 1.4 T. To avoid limitation through the field strength the field length of the sextupole can be increased which would lead to a lower ideal field strength for a given d and temperature. Simulations show that for $d = 25$ cm and 1 K the ideal field strength would be reduced from 1.4 T to about 0.9 T by increasing the field length from 10 cm to 15 cm. This and the results for 20 cm and 25 cm are shown in Fig. 3.9.

3.2.3. Gravity - Detector Size Studies

Fabrication of large Si-Detectors and handling of large area emulsions are problematic and limit the maximal sensitive detector area. At the moment it is not clear how large the detector will be. In the context of this issue the efficiency of detection associated with a certain detector size was examined by checking how many of the detected $\overline{\text{H}}$'s would have been in the area of a real detector.

Fig. 3.10 shows that 214 of the 287 $\overline{\text{H}}$'s (75 %) would be detected by an area of 10 × 10 cm². The detection efficiency reaches 100 % for a size of 12.5 × 12.5 cm² (Fig. 3.10, right).
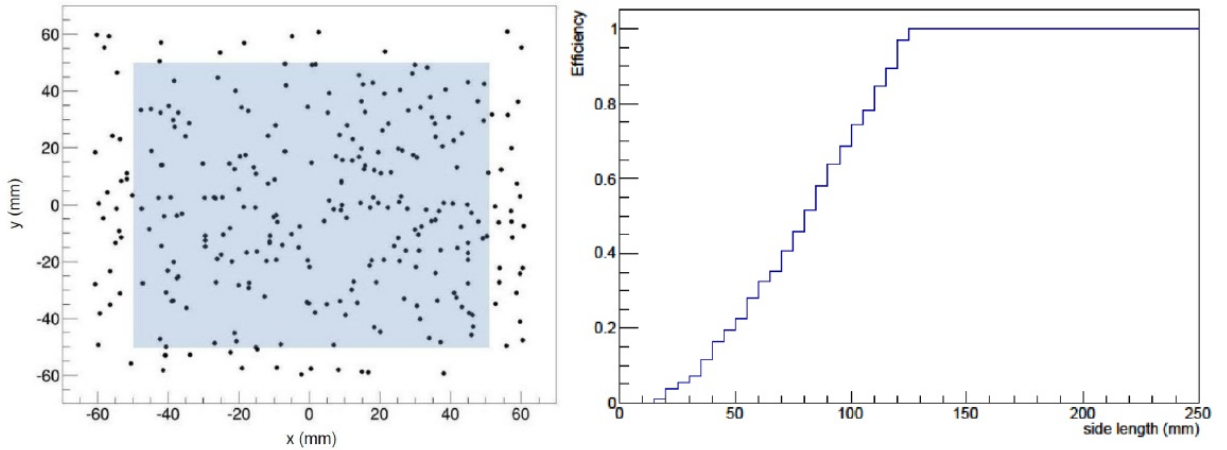

Figure 3.10.: Left: Detected position of 287 $\overline{\text{H}}$'s at the detector. The blue shadowed area corresponds to a detector area of 10 × 10 cm². Right: Dependence of efficiency on side length of the detector area.

3.3. Conclusion

The most important result of the beam optics simulations is that a sextupole magnet could increase the efficiency in the gravity experiment. A reduction in count rate will not result even if the magnet is not perfectly adapted to beam parameters like temperature. Apart from that the simulations show that a permanent magnet could provide enough focusing power for both experiments. These magnets can reach field strengths of around 1.4 T which is likely to be sufficient for temperatures of up to 1 K. From this point of view there is no need for a more expensive superconducting magnet. According to the simulations stronger focusing with permanent magnets can be achieved by increasing the field length.

A permanent sextupole would reduce the cost drastically in comparison to a superconducting one. The drawback of a permanent magnet is that its field strength cannot be tuned if beam parameters like temperature change.

Classical Trajectory Monte Carlo Simulations of AEGIS collaborators have shown that under the envisaged conditions for the $\overline{p}$'s and Ps each AD cycle (1 per 100 sec.) should lead to the formation of about 10 - 100 $\overline{H}$'s. According to simulations of TOF and position detectors a 1 % precision in g_{Hbar} will take about 10^5 produced $\overline{H}$'s at 0.1 K. This would correspond to some weeks or months of data taking if no sextupole magnet is used. [41]

A sextupole could reduce this time span according to the obtained gain in count rate (up to a factor of appr. 7).

4. Design and Construction of a Cryogenic Beam Line Shutter

4.1. Motivation and Specifications

In the 1 T trap e^-'s and $\bar{p}$'s will be exposed to thermal radiation that is emitted from the gravity or spectroscopy module. The temperatures will be at about 80 K for the gravity module and room temperature for the spectroscopy module. As pointed out in Section 2.2.3 a high temperature in these parts is beneficial since it accelerates the decay of the produced Rydberg $\bar{H}$'s into the ground state. A drawback of a higher temperature is that black body radiation from the warm parts will cause an increased heat load on the dilution refrigerator that keeps the inner walls of the 1 T trap at 0.1 K. According to calculations an experimental module at room temperature would result in a heat load on the 0.1 K region that exceeds the dilution refrigerator's cooling power by several orders of magnitude. [54]

Even if the inner walls of the 1 T trap are at 0.1 K the $\bar{p}$ temperature would be higher as the e^-'s in the trap would be heated by the black body radiation from the warmer parts of the experimental modules. This radiation propagates along the z direction and has therefore polarizations in the x-y plane. Therefore it couples to the cyclotron modes which describe the plasma's motion in this plane.

The ground state cyclotron mode of the e^-'s corresponds to a temperature of 0.65 K (see Section 2.2.1). Hence the transition energy from one mode to the next one can be associated with a temperature of about 1.3 K (see Eq. (2.3)). Black body radiation from the much warmer experimental modules would excite a considerable fraction of e^-'s into higher cyclotron states. Since the $\bar{p}$'s equilibrate quickly with the e^-'s in the plasma also their temperature would rise.

For $\bar{p}$'s the temperature corresponding to the cyclotron ground state is about 0.5 mK. But due to the lower charge to mass ratio the coupling of $\bar{p}$'s to the black body radiation from the warm experimental parts can be neglected. [55]

It is investigated whether a shutter blade could be used as a radiation shield for the cold $\bar{p}$ plasma. The blade would keep the downstream beam line of the 1 T trap closed as long as $\bar{p}$'s are trapped. The aperture to be covered by the shutter blade is about 20 cm in diameter. When the $\bar{H}$ formation process starts the shutter has to be opened. Prevention of $\bar{p}$ heating is especially crucial in the moments before $\bar{H}$ formation. Therefore the time it takes to open the shutter has to be as small as possible. Depending on the temperatures and geometries of the experiments the required time will vary. For the design of a prototype shutter some tens of ms are foreseen.

The temperature of the shutter blade should be below 20 K in order to sufficiently reduce the remaining black body radiation on the $\overline{\text{p}}$ plasma. A further challenge in the realization of this shutter is that it will be operated in the UHV region close to the cold $\overline{\text{p}}$ plasma. Therefore no lubricant can be used for its moving parts.

The most crucial requirement for the shutter is reliability. If the shutter gets stuck in its closed position it would not allow to extract any $\overline{\text{H}}$ from the source and would therefore stop the whole experiment. To repair the shutter it would be necessary to warm up the whole trap with its superconducting magnets at 4 K. This process takes weeks.
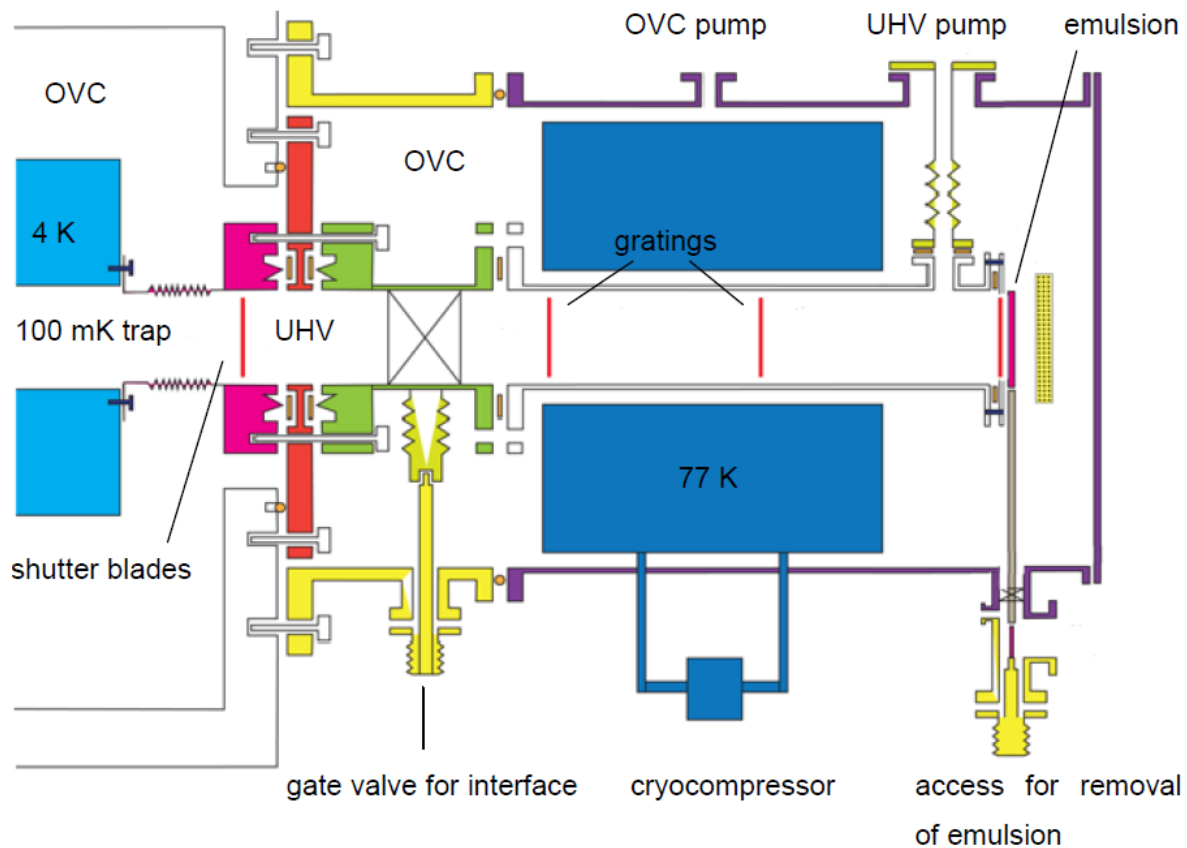

Figure 4.1.: Black body radiation from warmer experimental parts (the gravity module with the gratings is shown) may heat the cold plasma in the 1 T trap. The shutter would be located before the gate valve (yellow) of the interface. Adapted from [56]

4.2. Initial Design and Tests

Since the cryogenics and vacuum in the trap must not be distorted by the operation of the shutter it was decided to put the actuators in the Outter Vacuum Chamber (OVC, see Fig. 4.1). This vacuum is used for thermal insulation and is separated from the UHV in the $\overline{\text{H}}$ beam line. As a consequence a mechanical feed-through from the OVC to the

blades in the UHV is required. Actuation of the shutter blade will be driven by thrust magnets in the OVC. These magnets consist of a coil that contains a movable yoke. In its relaxed position the yoke is halfway inserted in the coil. Current in the coil pushes the yoke towards the coil's centre and therein moves it for about 2 cm. The force that is exerted on the yoke depends on the current in the coils. The feed-through will be attached to a yoke and transfer the motion to the shutter blade in the UHV. To move the shutter in the other direction (closing it) another magnet is used, which is operated in the opposite direction and also attached to the feed-through (see Fig. 4.3).

A magnet with suitable specifications (Kuhnke H6206-F-24VDC100%ED) was acquired and tested for its minimum actuation time in dependence of the applied voltage/current. To account for the inertia of the shutter blade a corresponding mass was attached to the yoke of the magnet. The magnet was driven by a standard lab power supply that allows a DC voltage of up to 60 V and currents up to 3 A. Using the maximum available voltage ($\sim$ 60 V) an actuation time of about 27 ms was achieved for a stroke length of 18 mm.

In order to avoid damage of the power supply a diode is connected in parallel to the magnets. Otherwise switching off the current in the magnet would lead to a self-induced voltage that may discharge in the power supply. The diode is back-biased as long as the power supply is turned on and hence all current passes through the magnet. After turning off a voltage in the opposite direction is induced. The resulting current can pass through the diode without harming the power supply.

The initial idea for the shutter blades was to use an iris. In comparison to a single large shutter blade this would reduce the required space for opening and closing. For tests a commercially available iris that is usually applied in optics experiments was used. First tests with the iris aimed at finding out how robust it is when opened or closed fast. In these tests the iris was driven by mechanical springs.

To measure the required time for opening two light barriers were used. Each of them consists of a laser diode/pointer and a photo diode. The amplified signal of the photo diodes was recorded by an oscilloscope. One light barrier passes through the outermost part of the iris and indicates when the iris is completely opened. The other one is placed at its centre and allows to determine when the shutter began to open (see Fig. 4.2).

Opening times of 10 ms were already achievable with this test setup. But after about ten openings at this speed one iris blade was slightly deformed. As result the iris got stuck in a half opened position.

A further problem with the iris was encountered in cooling tests. For this purpose the shutter was attached to a holding structure which ensures a large contact area to the iris' anodised aluminium frame. This holding structure was built at the work shop of the institute. It is mounted on a cold finger that is cooled by a helium cryocompressor. Springs push the iris frame against the holding structure to ensure that contact is not lost through thermal compression during the cool down. The whole test took place in a vacuum chamber with an ambient gas pressure of 10^{-7} mbar. As the walls of the vacuum chamber are at room temperature black body radiation would heat the iris. Therefore it was wrapped into several layers of highly reflective super-insulation foil. The temperature was measured on the cold finger with a silicon diode (DT-670) and at

the central point of the closed shutter blade with a PT-100 resistor. With a constant cold finger temperature of 10 K the iris reached a stationary temperature of 190 K. Since the only heat source on the iris was the remaining radiation this result indicates that cooling of the individual blades of an iris is not efficient. The main problem is that each blade is connected to the iris' frame only by a small bin that is stuck in a hole in the frame. When the iris is opened the blades rotate around this connection point. The small contact area that these connections provide limits the heat transport.
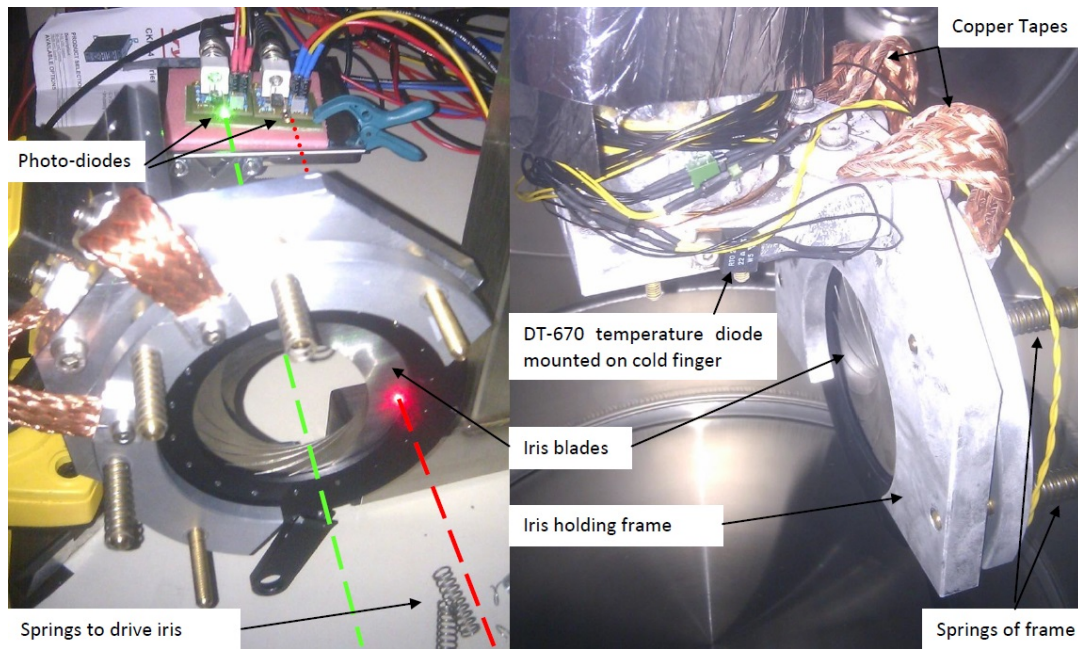
Figure 4.2.: Left: Light barriers (dashed lines) and an oscilloscope were used to measure the minimal opening time the iris allows. For this test elastic springs were used to drive the opening process. Times of about 10 ms were reached. This resulted in deformation of two iris blades which did not allow further operation and required disassembling in order to repair it. Right: During the cryotests the shutter was held by a frame that ensured contact throughout the cooling process by springs that are visible at the shutter's back side. Two copper tapes provided heat conduction from the holding frame to the cold finger.

4.3. Final Design and Test Setup for the Prototype

The problems with blade deformation and heat transport indicated that an iris shutter is not feasible. Due to the complexity of the iris mechanism (each of the 20 iris blades is slightly different in shape) this option was discarded.

A simpler design as shown in Fig. 4.3 was developed. As described above two magnets in the OVC are used to open and close the shutter. The rectangular shutter blades are

mounted on a bearing that allows rotation. The bearing is attached to a holding structure on a flange that can be installed into a vacuum chamber. A linear feed-through will transfer the motion from the magnets (one for closing, one for opening) in the OVC to the shutter blades in the UHV. The feed-through is made by a vacuum tight bellows that is attached on the OVC side of the flange. On the other side the bellows is vacuum tightly glued to a piston that can be moved back and forth by the magnets. Inside the bellows an aluminium bar establishes a connection from the piston to the shutter blade through a hole in the flange. If the magnets move the piston up the bellows is compressed and the bar transfers the motion to the rotating shutter blade. In the test of the shutter the blade rotates about 38° from the closed position to the opened position. This value is determined by the maximum rotation the mechanism allows and the relaxed position of the bellows. In order to uncover a beam pipe completely with four shutters 66° will be necessary. This will require to add a holding mechanism that restores the shutter in its closed position and keeps the bellows slightly stretched. The initial tests with the prototype do not aim at this issue but are rather a feasibility study of a cold shutter in general.
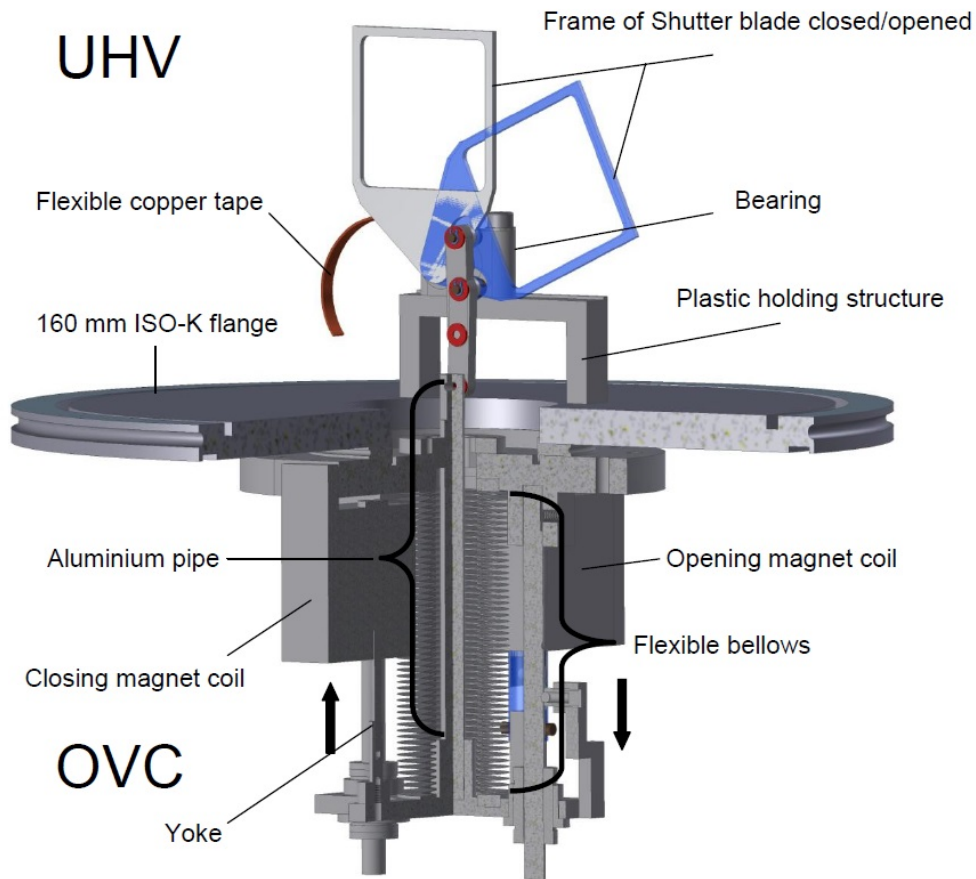

Figure 4.3.: Technical drawing of the final design of the shutter prototype. See text for details. Drawn by D. Stückler (SMI).

Depending on the size of each shutter blade either two or four of them will be required to cover the whole beam pipe. The shutter blades are made of stainless steel frames that will be covered by a highly reflective metal foil (e.g. gold). For cooling a copper tape establishes a connection from a cold finger to the shutter blade. The tape is attached to the copper connection of the blade with the bearing. This position close to the rotation axis was chosen in order to reduce the momentum of inertia. To minimize heating of the copper tape through thermal radiation the tape was wrapped in three layers of super insulation.

The structure that holds the bearing and the blade on the flange is made of plastic. Initially it was made of stainless steal but to reduce heat conduction it was later replaced by plastic parts.

The prototype was build in the work shop of the Stefan-Meyer Institute. First tests of the magnets, the feed-through and the rotation mechanism were made outside a vacuum chamber. The minimum opening time was found to be 23 ms at 60 V and about 1 A.
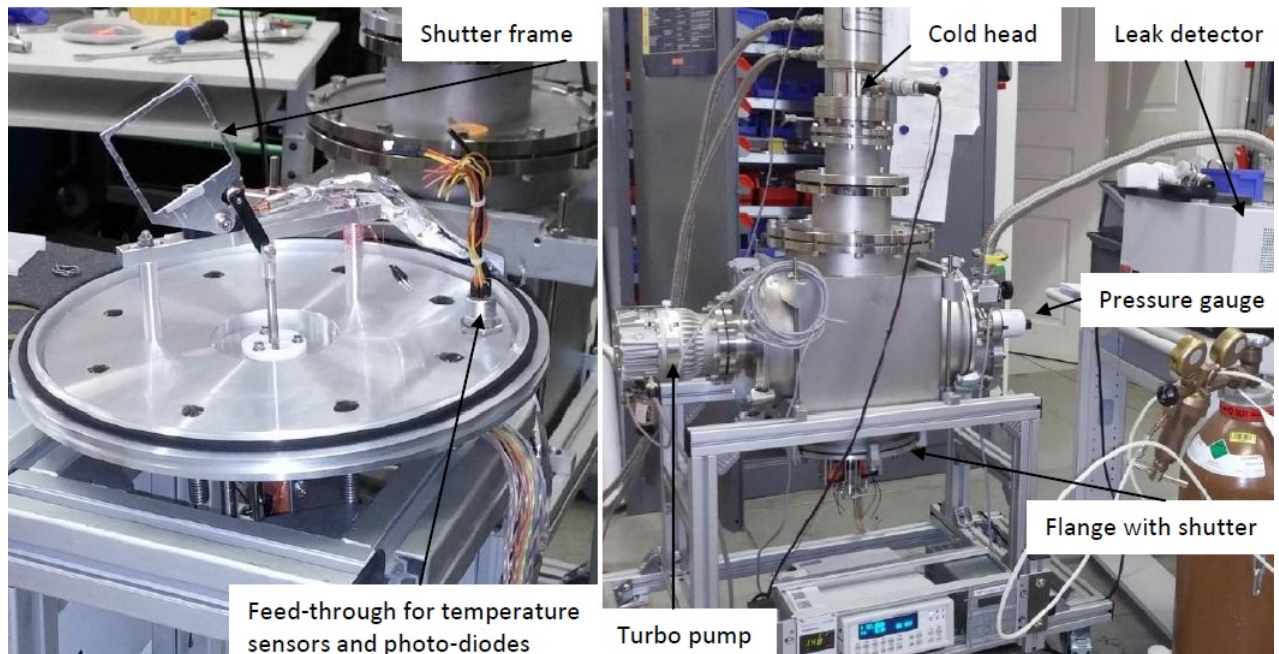
Figure 4.4.: Left: The prototype shutter placed outside the vacuum chamber for leak tightness testing. Right: The shutter installed on the bottom of the vacuum chamber, the coils (orange) are visible. On top of the chamber the cold head is mounted with connection cables to the helium cryocompressor. At the right hand side the pressure gauge and the entrance window for the laser light of the light barrier are attached. Above the pressure gauge a valve was used to connect the helium leak detector with the chamber. This allowed to test the complete vacuum chamber for leaks. The turbo pump is mounted on the left hand side.

A helium leak detector was used to check the feed-throughs and glued screw connections (black spots on the shutter flange in Fig. 4.4) on the flange of the shutter. For this purpose an o-ring was placed around the spot that is to be checked. The small flange of the tube of the helium leak detector was placed on this o-ring which fits the flange's dimension. Then an injection needle was used to apply ethanol to the contact surface of the shutter flange and the o-ring. When the turbo pump in the leak detector is turned on the pressure drop inside the tube freezes the ethanol and therein makes the o-ring leak tight. Helium was blown on the investigated spot from the other side of the shutter's flange. If there is a leak the helium will get sucked in by the turbo pump of the leak detector and be detected by a sector magnet spectrometer. Next the shutter was put into a vacuum chamber and leak tightness of the whole setup was checked (see Fig. 4.4 right).
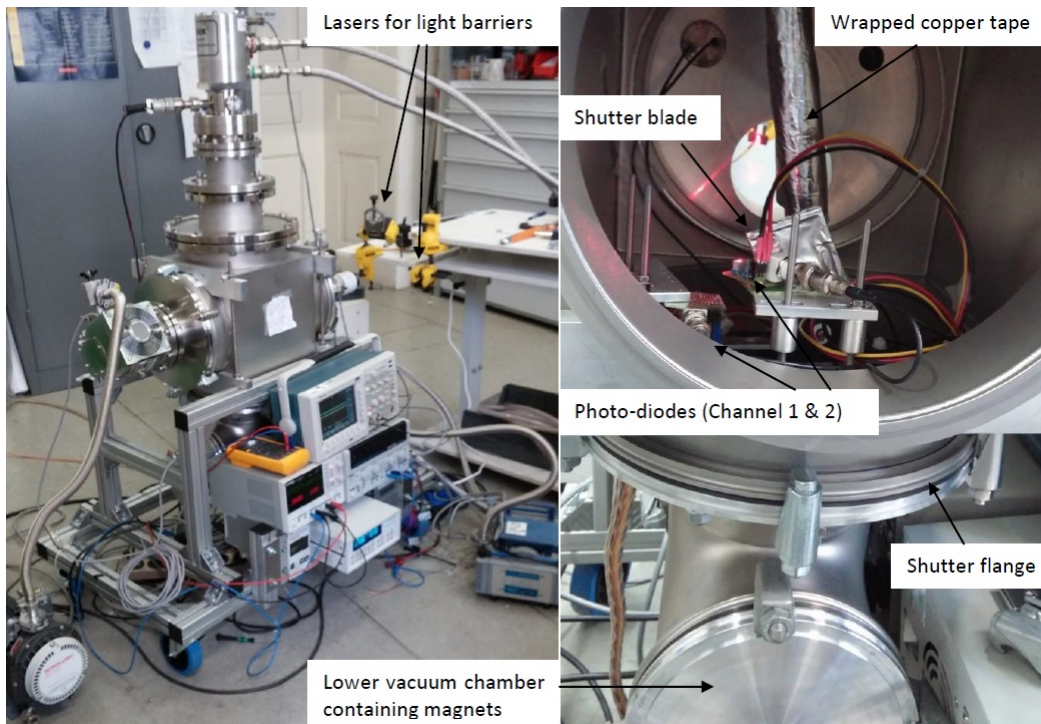

Figure 4.5.: Left: The complete setup. On the white table two yellow bench vices hold the lasers for the light barriers. Right: The shutter installed in the vacuum chamber. In the fore ground one of the photo diodes is visible on an amplifier board. The cabling of the amplifiers includes the power supply in black and red and ground in yellow. The amplifier signal is transmitted with a BNC cable whose feed-through is visible left above the window. The second amplifier board is half visible on the left hand side of the other one. Due to the very limited space in the chamber it had to be mounted upside down. Through the window a laser diode is visible that shines red light on one of the photo-diodes. Wrapped in super insulation foil the cooper tape connects the shutter with the cold finger on top.

Schnitt A-A
M 1 : 2

Cold head

267.00

56.00

56.00

291.00

150.00

1192.10

B

B

A

A

416.00

1192.10

Schnitt B-B
M 1 : 2

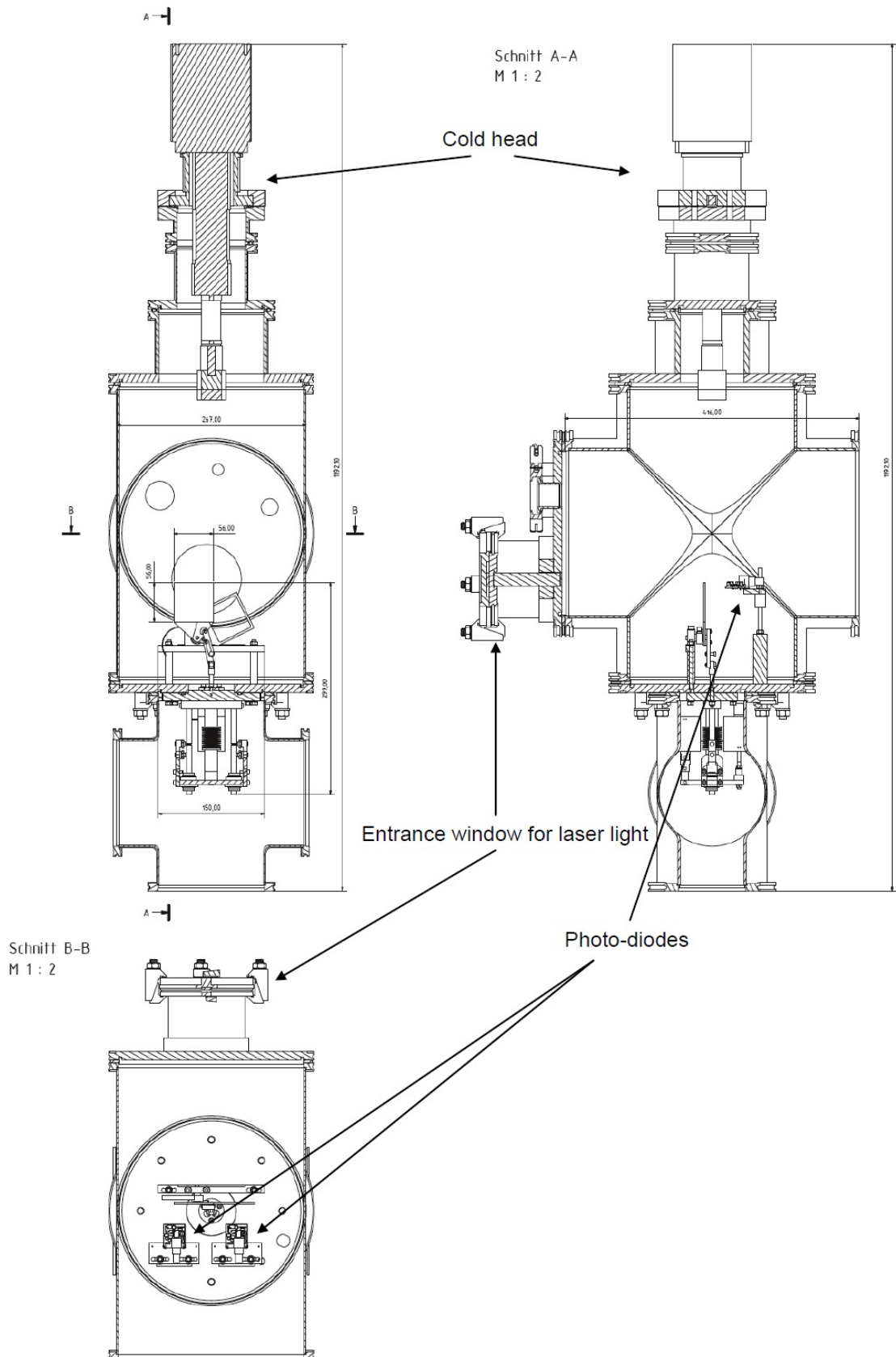Entrance window for laser light

Photo-diodes

Figure 4.6.: Technical drawing of the shutter test setup as shown in Fig. 4.4 and Fig. 4.5. Drawn by Doris Stückler (SMI).

Finally the photo-diodes were glued on the flange (see Fig. 4.6) and adjusted to be in the right position to detect the laser rays. Temperature sensing diodes (DT-670) were attached on the shutter frame and the cold finger to monitor the temperature.

To examine how far the shutter can be cooled down the cold finger was cooled to 10 K and the ambient gas pressure was about 4×10^{-7} mbar. After several hours the shutter reached a stable temperature of 163 K.

To examine the opening times that the shutter can achieve at low temperatures also the lower part of the flange that carries the shutter has to be in vacuum. Otherwise the lower pressure inside the chamber would keep the bellows contracted and hinder the shutter from moving. A smaller vacuum chamber was attached to the bottom side of the shutter flange and evacuated (see Fig. 4.5 right, bottom).
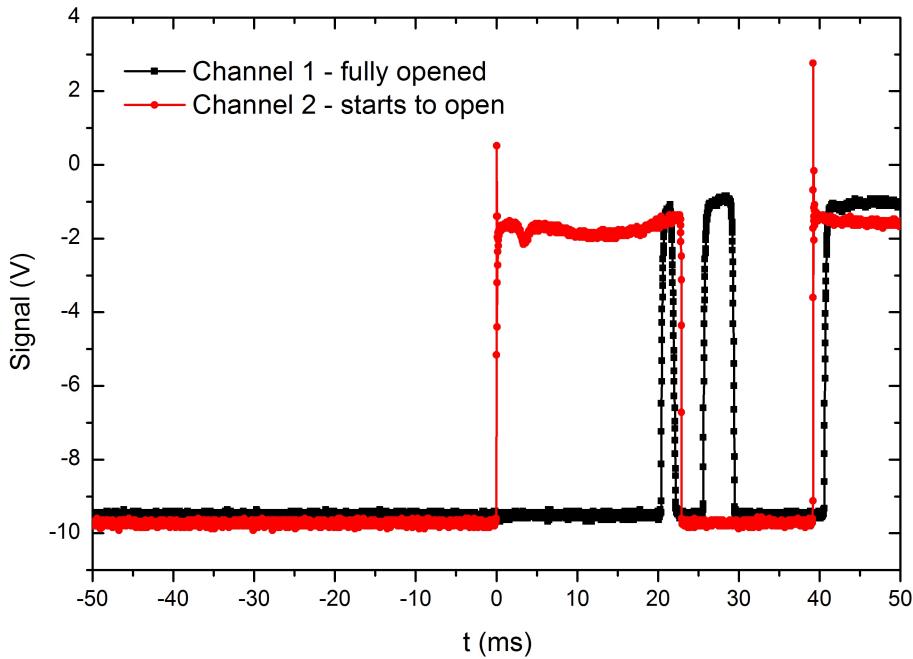

Figure 4.7.: Signals of the light barriers that indicate when the shutter begins to open (channel 2) and when it is fully opened (channel 1). The position of the photo-diode and the laser for channel 2 can be seen in Fig. 4.5 right and in Fig. 4.6. The measurement was made at room temperature. At the moment when the shutter covers the photo-diodes the signal of the corresponding channel rises. The opening time of 23 ms is determined as the time span between the rise of the signals of channel 2 and channel 1. It can be seen that the photo-diode of channel 1 is not immediately stable but has two peaks. When the shutter reaches the fully opened position its motion is abruptly stopped because the yoke in the magnet can not move further. Due to the resulting rebound of the shutter blade the photo-diode of channel 1 gets uncovered again for a short time. In this way the peaks are caused before the shutter stays in the fully opened position and the signal is stable.

At 163 K the lowest opening time was 16 ms (Fig. 4.8). To further improve cooling the copper tape was glued directly on the shutter and a second copper tape was used in parallel. This way the lowest temperature reached was 70 K. At this temperature the shutter was not moved quickly since this may have broken the glued connection to the copper tape. Due to the result in Fig. 4.8 it is expected that the opening time does not get longer with lower temperature. In future designs a robust connection from the shutter to the copper tape shall be foreseen.

Fig. 4.7 shows a drop in the signal of channel 2 after the shutter is closed. This is unexpected and needs further investigation.
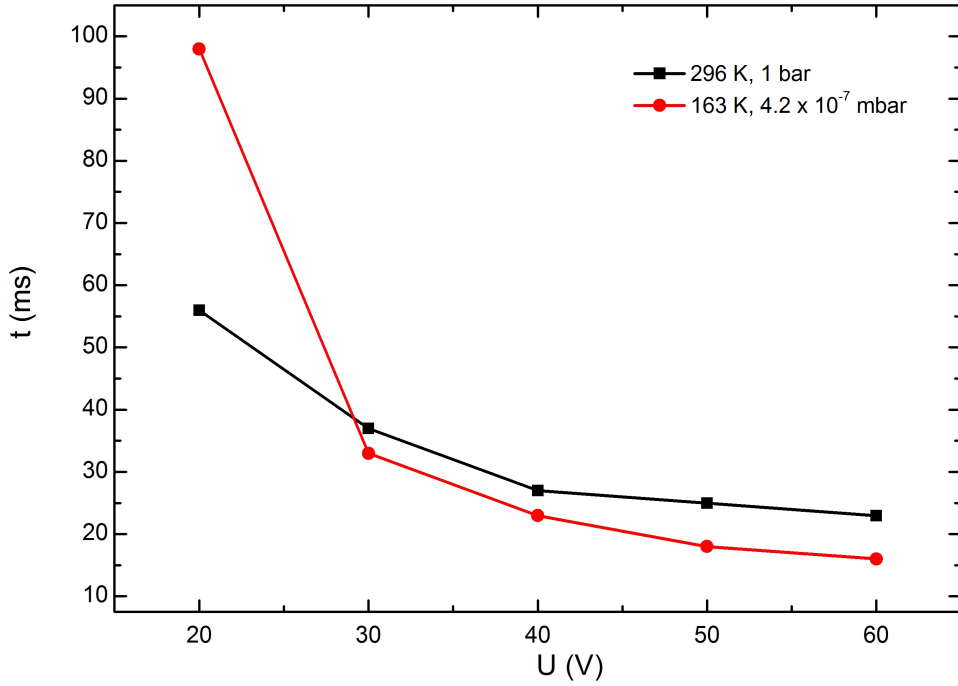

Figure 4.8.: Opening times for room temperature and 163 K in dependence of applied voltage. The current at 30 V is 0.52 A and at 60 V it is 0.95 A. For 20 V the opening time is very different for the two temperatures. This may be attributed to thermal contraction that causes additional friction. For higher voltages this seems to be negligible as the magnet's force is stronger. In these cases the cold shutter in vacuum was slightly faster.

In the following section the heat load through thermal radiation and heat conduction are estimated. Analogue considerations may show whether the goal of 20 K shutter temperature in the environment of the gravity and spectroscopy module are realistic with the current design.

To calculate the stationary heat conduction Fourier's law is used:

$$P_{Con} = \frac{\lambda}{l} A(T_1 - T_2). \tag{4.1}$$

Here P is the transmitted heat power and λ the thermal conductivity. l is the length and A the cross section that conducts the heat flow. $T_{1,2}$ are the temperatures of the thermal reservoirs under consideration.

The shutter components that are taken into account for heat conduction are the plastic holding structure, the aluminium pipe and the copper tape (see Fig. 4.3). In the test of the prototype the cold finger was at 10 K and the shutter reached a constant temperature of 70 K. The magnets and the flange were at room temperature ($\approx$ 300 K). With these temperatures the following heat conduction P to the shutter is calculated:

Component	λ	l (cm)	A (cm^2)	T1 (K)	T2 (K)	P_{Con}(W)
Plastic Holding Structure	0.2	6	1	300	70	0.08
Aluminium Pipe	236	15	0.01	300	70	0.36
Copper Tape	400	30	0.1	10	70	-0.80
						-0.36

Table 4.1.: Estimated heat conduction in the prototype setup.

The heat load on the shutter blade[1] arising from black body radiation in the vacuum chamber is calculated with the Stefan-Boltzmann law:

$$P_{Rad} = \sigma A(\epsilon_1 T_1^4 - \epsilon_2 T_2^4). \tag{4.2}$$

The emissivity for the inner walls of the vacuum chamber (rough aluminium) is estimated to be $\epsilon_1 = 0.07$ and for the shutter blade wrapped in aluminium foil $\epsilon_2 = 0.04$. $\sigma = 5.67 \times 10^{-8} \frac{W}{m^2 K^4}$ is the Stefan-Boltzmann constant. The surface area (both sides) A of the shutter is 60 cm^2. $T_1 = 300$ K is the temperature of the surrounding wall and T_2 = 70 K of the shutter blade. A view factor that takes into account the alignment and geometry of the radiating surfaces (walls and shutter blade) was omitted for simplicity of the estimation.

Using these values the radiative heat flow is calculated to be 0.2 W.

In the stationary state the heat flows through the shutter have to sum up to zero

$$\sum P_{Con} + P_{Rad} = 0. \tag{4.3}$$

For the estimation this condition does not hold exactly: $0.08+0.36-0.8+0.2 = -0.16$ W. This result indicates that in the estimation the shutter would still emit heat and therein become cooler.

To which shutter temperature T_s it would cool down under the estimated conditions can be calculated by imposing Eq. (4.3). Expressing (4.3) in terms of the variable T_s and solving it gives:

$$\frac{0.2}{0.06} \times 10^{-4} \times (300 - T_s) + \frac{236}{0.15} \times 10^{-6} \times (300 - T_s) + \frac{400}{0.3} \times 10^{-5} \times (10 - T_s) +$$
$$5.67 \times 10^{-8} \times 60 \times 10^{-4} \times (0.07 \times 300^4 - 0.04 \times T_s^4) = 0 \rightarrow T_s = 59.0\ K. \tag{4.4}$$

---

[1]Radiative heat load on the copper tape was neglected since the tape was wrapped in several layers of super insulation foil.

Thus the estimated dimensions, heat conductances and radiative heat load would result in a temperature that is about 11 K lower than in reality. This shows that either the heat load on the shutter is underestimated or the cooling power is overestimated.

An analogues equation can be used for conditions that may be present if the gravity module is attached. In this case the following boundary conditions are assumed:

- 80 K temperature of the flange and the magnets,

- 4 K temperature of a cold finger which is connected to the copper tape.

- radiative heat load of 80 K black body radiation on only one side of the shutter

The corresponding equation for T_s and its solution are:

$$
\frac{0.2}{0.06} \times 10^{-4} \times (80 - T_s) + \frac{236}{0.15} \times 10^{-6} \times (80 - T_s) + \frac{400}{0.3} \times 10^{-5} \times (4 - T_s) +
$$
$$
5.67 \times 10^{-8} \times 30 \times 10^{-4} \times (0.07 \times 80^4 - 0.04 \times T_s^4) = 0 \rightarrow T_s = 13.5 \ K. \tag{4.5}
$$

Although it is known that the estimation provides shutter temperatures that are too low this is quite promising.

In case of the spectroscopy module the only difference with respect to the gravity module is that the black body radiation has a temperature of 300 K. The obtained estimation for the shutter temperature is 19.8 K. Also here it seems to be possible to achieve 20 K. If for instance the copper tape is taken twice the estimation would result in 12.4 K.

4.4. Conclusion

The prototype demonstrated a feasible way to construct a beam line shutter for AEGIS. The envisaged opening time of some tens of ms will to be possible. Lower times may be reached by replacing the lab power supply by a dedicated device with higher power.

The estimations of the heat flows show that the cooling power achieved with copper tapes (eventually taken twice) should be sufficient to reach less than 20 K shutter temperature with both modules (gravity and spectroscopy).

In the AEGIS beam line the recoil of the shutter may cause notable vibration of the whole setup. This is critical for the gravity measurement since here the vertical position of the $\overline{\mathrm{H}}$'s is detected with a resolution of a few μm. For this reason the shutter shall be installed in a way that its recoil is along a horizontal direction. In addition methods to reduce the vibrations should be foreseen.

A. Appendix

A.1. Commutation Relations for H_{HFS} and Calculation of Hyperfine States

In order to show that $[F_z, H_{HFS}] = 0$ the usual commutation relations among the components of a general angular momentum operator $[J_i, J_j] = i\hbar\epsilon_{ijk}J_k$ are used and that all components of $\mathbf{I}$ commute with those of $\mathbf{S}$:

$$[F_z, \mathbf{IS}] = [F_z, I_x S_x + I_y S_y + I_z S_z] = [S_z, I_x S_x + I_y S_y] + [I_z, I_x S_x + I_y S_y] = \\ i\hbar(I_x S_y - I_y S_x)) - i\hbar(I_x S_y - I_y S_x) = 0. \tag{A.1}$$

The same arguments are sufficient to calculate the remaining commutator:

$$[F_z, (aS_z + bI_z)B_z] = [S_z + I_z, (aS_z + bI_z)B_z] = 0. \tag{A.2}$$

Next it shall be shown that $B \neq 0 \to [F^2, H_{HFS}] \neq 0$.

$$[F^2, H_{HFS}] = [\mathbf{S}^2 + \mathbf{I}^2 + 2\mathbf{IS}, A\,\mathbf{IS} + (aS_z + bI_z)B_z] \tag{A.3}$$

Vanishing of $[\mathbf{S}^2 + \mathbf{I}^2, A\,\mathbf{IS}]$ follows directly from $[\mathbf{S}^2, \mathbf{S}] = [\mathbf{S}^2, \mathbf{I}] = 0$ and the equivalent relations for $\mathbf{I}^2$.
$[A\,\mathbf{IS}, 2\mathbf{IS}] = 0$ requires no further considerations.
If $B = 0$ this is sufficient to show that $[F^2, H_{HFS}] = 0$. Otherwise the commutators containing $(aS_z + bI_z)B_z$ have to be calculated:

$$[F^2, (aS_z + bI_z)B_z] = [(I_x + S_x)^2 + (I_y + S_y)^2 + (I_z + S_z)^2, (aS_z + bI_z)B_z] \\ [(I_x + S_x)^2 + (I_y + S_y)^2, (aS_z + bI_z)B_z]. \tag{A.4}$$

Just commutators involving only components of either $\mathbf{S}$ or $\mathbf{I}$ may not vanish. As an example the following commutator is calculated:

$$[(I_x + S_x)^2, aS_z] = [S_x^2, aS_z] + [2I_x S_x, aS_z]. \tag{A.5}$$

Using $[J_i, J_j] = i\hbar\epsilon_{ijk}J_k$ one obtains:

$$[S_x^2, aS_z] = S_x[S_x, aS_z] + [S_x, aS_z]S_x = -i\hbar a(S_x S_y + S_y S_x). \tag{A.6}$$

This cancels with:

$$[S_y^2, aS_z] = S_y[S_y, aS_z] + [S_y, aS_z]S_y = i\hbar a(S_x S_y + S_y S_x). \tag{A.7}$$

Similarly also all other commutators in (A.4) that contain a squared component of $\mathbf{S}$ or $\mathbf{I}$ vanish. Finally the remaining commutators are:

$$
\begin{aligned}
[I_x S_x, a S_z] &= -i\hbar a I_x S_y \\
[I_y S_y, b I_z] &= i\hbar b I_x S_y \\
[I_x S_x, b I_z] &= -i\hbar b I_y S_x \\
[I_y S_y, a S_z] &= i\hbar a I_y S_x
\end{aligned}
\tag{A.8}
$$

Since $a \neq b$ these terms do not cancel.

Calculation of $m = 0$ Hyperfine States

To calculate the eigenstate that belongs to the eigenvalue $E_{m=0}^+$ in (3.7) the following system of linear equations needs to be solved:

$$
\begin{pmatrix} -A + 2B(a-b) - 4E_{m=0}^+ & 2A \\ 2A & -A - 2B(a-b) - 4E_{m=0}^+ \end{pmatrix} \begin{pmatrix} x \\ y \end{pmatrix} = \begin{pmatrix} 0 \\ 0 \end{pmatrix}.
\tag{A.9}
$$

Here x and y are the components of the eigenvector in the $|\frac{1}{2}, -\frac{1}{2}\rangle, |-\frac{1}{2}, \frac{1}{2}\rangle$ basis. Solving this equation and using the abbreviation $s = (a-b)B$ the following relation is obtained:

$$
x = \frac{1}{A}(s + \sqrt{s^2 + A^2})\, y.
\tag{A.10}
$$

From that the norm N of these states is determined to be:

$$
N = \sqrt{1 + \frac{s^2 + 2s\sqrt{s^2 + A^2} + s^2 + A^2}{A^2}} = \frac{\sqrt{2}}{A}\sqrt{A^2 + s^2 + s\sqrt{s^2 + A^2}}.
\tag{A.11}
$$

Thus the vectors

$$
\frac{1}{N} \begin{pmatrix} \frac{1}{A}(s + \sqrt{s^2 + A^2}) \\ 1 \end{pmatrix}.
\tag{A.12}
$$

are the eigenvectors in the basis defined above. Inserting the found expression for N one obtains for the y component:

$$
y = \frac{1}{\sqrt{2}}\sqrt{\frac{A^2 + x^2 - s\sqrt{A^2 + s^2}}{A^2 + s^2}} = \sqrt{\frac{1}{2} - \frac{s}{\sqrt{s^2 + A^2}}} = \sqrt{\frac{1 - \cos(\alpha)}{2}} = \sin(\frac{\alpha}{2}), \quad \text{(A.13)}
$$

where $\alpha = \arctan(\frac{A}{s})$. Using the normalization condition $x^2 + y^2 = 1$ the x component is immediately found to be $\cos(\frac{\alpha}{2})$.

Since the the eigenvector of the second eigenvalue $E_{m=0}^-$ needs to be orthogonal to the one that was calculated above the following relations for its components v and w are obtained:

$$
\begin{pmatrix} v \\ w \end{pmatrix} \begin{pmatrix} \cos(\frac{\alpha}{2}) \\ \sin(\frac{\alpha}{2}) \end{pmatrix} = 0 \rightarrow v = -w\frac{\sin(\frac{\alpha}{2})}{\cos(\frac{\alpha}{2})}.
\tag{A.14}
$$

Using the normalization condition for this state the components are obtained:

$$
1 = v^2 + w^2 = w^2 \frac{\sin^2(\frac{\alpha}{2})}{\cos^2(\frac{\alpha}{2})} + w^2 \rightarrow w^2 \left(\sin^2(\frac{\alpha}{2}) + \cos^2(\frac{\alpha}{2}) \right) \rightarrow w = \cos(\frac{\alpha}{2}).
\tag{A.15}
$$

Using (A.14) the second component v is found to be $-\sin(\frac{\alpha}{2})$.

List of Figures

List of Tables

Bibliography

[1] Greiner, W. *Relativistic Quantum Mechanics.* (Springer Verlag, Berlin, 2000).

[2] Peskin, M. & Schroeder, D. *An Introduction to Quantum Field Theory.* (Westview Press, New York, 1995).

[3] Wagner, T. A. *et al.* Torsion-balance tests of the weak equivalence principle. *Classical Quant. Grav.* **29**, *184002* (2012).

[4] Paschos, E. *Electro Weak Theory.* (Cambridge University Press, New York, 2007).

[5] Alves, D. S. M. *et al.* Experimental constraints on the free fall acceleration of antimatter. (2009). Preprint at http://arxiv.org/abs/0907.4110.

[6] Rugh, S. & Zinkernagel, H. The quantum vacuum and the cosmological constant problem. *Downloaded on 25.4.2014 from: http://philsci-archive.pitt.edu/id/eprint/398* (2001).

[7] Gabrielse, G. *et al.* Precision mass spectroscopy of the antiproton and proton using simultaneously trapped particles. *Phys. Rev. Lett.* **82**, *3198-3201* (1999).

[8] Hughes, R. J. & Holzscheiter, M. H. Constraints on the gravitational properties of antiprotons and positrons from cyclotron-frequency measurements. *Phys. Rev. Lett.* **66**, *854-857* (1991).

[9] Fischler, M. *et al.* Direct observation limits on antimatter gravitation. (2008). Preprint at http://arxiv.org/abs/0808.3929.

[10] Morrison, P. Approximate nature of physical symmetries. *Am J Phys* **26**, *358-368* (1958).

[11] Kostelecky, V. & Tasson, J. Matter-gravity couplings and Lorentz violation. *Phys. Rev. D* **83**, *016013* (2011).

[12] Harrison, P. Nature's flawed mirror. *Phys. World* **16N7**, *27-31* (2003).

[13] Sozzi, M. *Discrete Symmetries and CP Violation - From Experiment to Theory.* (Oxford University Press, New York, 2008).

[14] Steigman, G. When clusters collide: Constraints on antimatter on the largest scales. (2008). Preprint at http://arxiv.org/abs/0808.1122.

[15] Cohen, A. G. *et al.* A matter - antimatter universe? *Astrophys. J.* ***495***, *539-549* (1998).

[16] Villata, M. CPT symmetry and antimatter gravity in general relativity. *EPL* ***94***, *20001* (2011).

[17] Benoit-Lévy, A. & Chardin, G. Do we live in a "Dirac-Milne" universe? (2009). Preprint at http://arxiv.org/abs/0903.2446.

[18] Hajdukovic, D. Is dark matter an illusion created by the gravitational polarization of the quantum vacuum? *Astrophys Space Sci* ***334***, *215-218* (2011).

[19] Charman, A. E. Description and first application of a new technique to measure the gravitational mass of antihydrogen. *Nat. Commun.* ***4***, *1785* (2013).

[20] Kellerbauer, A. *et al.* The AEGIS experiment at CERN. *Hyperfine Interact* ***209***, *43-49* (2012).

[21] Debu, P. Status report on the GBAR CERN experiment. *J. Phys. Conf. Ser.* ***460***, *0120* (2013).

[22] Lüders, G. On the equivalence of the invariance under time reversal and under particle-antiparticle conjugation. *Dansk. Mat. Fys. Medd.* ***28***, *5* (1954).

[23] Pauli, W. *Exclusion principle, Lorentz group and reflection of space-time and charge.* (Pergamon Press, New York, 1955).

[24] Álvarez-Gaumé, L. & Vázquez-Mozo, M. *An Invitation to Quantum Field Theory.* (Springer Verlag, Berlin, 2012).

[25] Bluhm, R. *et al.* CPT and Lorentz tests in hydrogen and antihydrogen. *Phys. Rev. Lett.* ***82***, *2254* (1999).

[26] Colladay, D. & Kostelecký, V. A. CPT violation and the Standard Model. *Phys. Rev. D* ***55***, *6760* (1998).

[27] Widmann, E. *et al.* Letter of intent for AD: Measurement of the anithydrogen hyperfine structure. *CERN-SPSC-2003-009, Downloaded on 3.4.2014 from: http://www.antimaterie.at/publications/project-materials.html* (2003).

[28] Bertolami, O. *et al.* CPT violation and baryogenesis. (1996). Preprint at http://arxiv.org/abs/hep-ph/0205279.

[29] Widmann, E. *et al.* Measurement of the hyperfine structure of antihydrogen in a beam. *Hyperfine Interact* ***215***, *1-8* (2013).

[30] Krasnický, D. Measuring gbar with AEGIS. *Talk at the Workshop on Antimatter Gravity, Bern* (2013).

[31] Madsen, N. *et al.* Spatial distribution of cold antihydrogen formation. *Phys. Rev. Lett.* **94**, *033403* (2005).

[32] Storry, C. *et al.* First laser-controlled antihydrogen production. *Phys. Rev. Lett.* **93**, *263401* (2004).

[33] Storey, J. *et al.* Towards the production of an ultra cold antihydrogen beam with the AEGIS apparatus. *Hyperfine Interact* **212**, *109-116* (2011).

[34] Doser, M. *et al.* Proposal for the AEGIS experiment at the CERN atiproton decelerator. *CERN-SPSC-2007-017, Downloaded on 4.3.2014 from: aegis.web.cern.ch/aegis/Proposal/Proposition.pdf* (2007).

[35] Malmberg, J. H. & Driscoll, C. F. Long-time containment of a pure electron plasma. *Phys. Rev. Lett.* **44**, *654* (1980).

[36] Braeunig, P. Moire deflectometry with atoms and antiatoms. *Talk at the Workshop on Antimatter Gravity, Bern* (2013).

[37] Canali, C. *et al.* Off-axial plasma displacement suitable for antihydrogen production in AEgIS experiment. *Eur. Phys. J. D* **65**, *499-504* (2011).

[38] Caravita, R. Laser apparatus for exciting positronium in AEGIS positronium spectroscopy experiment. *Diploma Thesis at University of Pavia* (2011).

[39] UCSD. Picture taken from homepage of positron research group. *Downloaded on 23.4.2014 from: http://positrons.ucsd.edu/positron/trappingframe.html.* .

[40] Jorgenson, L. *et al.* The AEgIS antihydrogen gravity experiment. *Hyperfine Interact* **212**, *41-49* (2011).

[41] Doser, M. *et al.* AEGIS: An experiment to measure the gravitational interaction between matter and antimatter. *J. Phys. Conf. Ser.* **199**, *012009* (2010).

[42] Galitski, V. *et al. Exploring Quantum Mechanics.* (Oxford University Press, Oxford, 2013).

[43] Testera, G. *et al.* Formation of a cold antihydrogen beam in AEGIS for gravity measurements. *AIP Conf. Proc.* **1037**, *5* (2008).

[44] Smirnov, B. *Physics of Atoms and Ions.* (Springer Verlag, New York, 2003).

[45] Haupert, F. *Dissertation: "A Moire-Deflectometer as Gravimeter for Antihydrogen".* (Ruperto-Carola-University of Heidelberg, 2012).

[46] Juhász, B. *et al.* Measurement of the ground-state hyperfine splitting of antihydrogen. *J. Phys. Conf. Ser.* **335**, *012059* (2011).

[47] Oh, S. *et al.* Entanglement, Berry phases, and level crossings for the atomic Breit-Rabi Hamiltonian. *Phys. Rev. A* **78**, *062106* (2008).

[48] Cohen-Tannoudji, C. *et al. Quantenmechanik Band 1 und 2.* (Walter de Gruyter, Berlin, 2007).

[49] gen. Schick, H. P. *et al. Nuclear Physics with Polarized Particles.* (Springer Verlag, New York, 2012).

[50] Agostinelli, S. *et al.* Geant4: a simulation toolkit. *Nucl. Instr. Meth. Phys. Res. A* **506**, *250-303* (2003).

[51] Antcheva, I. *et al.* ROOT - A C++ framework for petabyte data storage, statistical analysis and visualization. *Comput. Phys. Commun.* **180**, *2499-2512* (2009).

[52] Malbrunot, C. *et al.* Spectroscopy apparatus for the measurement of the hyperfine structure of antihydrogen. *Hyperfine Interact (2014), DOI: 10.1007/s10751-014-1013-z* .

[53] Press, W. *et al. Numerical Recipes - The Art of Scientific Computing.* (Cambridge University Press, New York, 2007).

[54] Derking, J. *Internal Note: "AEgIS: Radiative heat load from the measurement section".* (2013).

[55] F.Castelli. *Private Communication and Internal Note: "Trapped Electrons and Blackbody Radiation".* (2014).

[56] Amsler, C. *et al.* Measuring g for antimatter. *Talk at AEC Plenary Meeting (University of Bern), Bern* (2012).